



Water Resources Research

RESEARCH ARTICLE

10.1029/2022WR034339

Key Points:

- Fracture network tomography in a deep reservoir is achieved by joint microseismicity and thermal data inversion
- A robust and computationally efficient framework is established to fuse microseismic data and temperature data in the joint inversion
- · Fracture geometry is delineated explicitly, resulting in high-precision temperature prediction in demonstrated enhanced geothermal

Correspondence to:

Z. Jiang, jiangzhenjiao@hotmail.com

Citation:

Jiang, Z., Ringel, L. M., Bayer, P., & Xu, T. (2023). Fracture network characterization in reservoirs by joint inversion of microseismicity and thermal breakthrough data: Method development and verification. Water Resources Research, 59, e2022WR034339. https:// doi.org/10.1029/2022WR034339

Received 20 DEC 2022 Accepted 23 AUG 2023

Author Contributions:

Conceptualization: Zhenjiao Jiang Formal analysis: Zhenjiao Jiang, Lisa Maria Ringel, Peter Bayer, Tianfu Xu Funding acquisition: Peter Bayer, Tianfu Xu

Methodology: Zhenjiao Jiang, Lisa Maria Ringel

Software: Zhenjiao Jiang Validation: Zhenjiao Jiang, Lisa Maria Ringel, Peter Bayer

Writing - original draft: Zhenjiao Jiang Writing - review & editing: Lisa Maria

Ringel, Peter Bayer

Inversion of Microseismicity and Thermal Breakthrough Data: Method Development and Verification

Fracture Network Characterization in Reservoirs by Joint

Zhenjiao Jiang¹, Lisa Maria Ringel², Peter Bayer², and Tianfu Xu¹

¹Key Laboratory of Groundwater Resources and Environment, Ministry of Education, College of Environment and Resources, Jilin University, Changchun, China, ²Applied Geology, Institute of Geosciences and Geography, MLU Halle-Wittenberg, Halle (Saale), Germany

Abstract The spatial configuration of fractures often regulates flow and transport in the subsurface. However, the characterization of fracture networks is a challenging task, especially in deep reservoirs, because here only a limited number of boreholes is available to perform downhole logs and cross-well hydraulic and tracer tests. In this study, we develop a joint inversion procedure to infer fracture number, geometry, and aperture based on Bayesian principles, utilizing microseismic (MS) events and thermal breakthrough data; both are typically available in enhanced geothermal systems and unconventional gas/oil reservoirs. A basic discrete fracture geometry, including orientations, lengths and positions of fractures, is generated from an MS events cloud by minimizing the distance between fractures and MS events. This geometric configuration, together with the aperture, is then further adjusted, based on the reversible jump Markov chain Monte Carlo algorithm, to minimize the misfit between observed and calculated thermal breakthrough curves by iterative forward flow and heat transport modeling. The inversion model is applied to two synthetic test cases. Following the sensitivity analysis of temperatures to fracture parameters, and the robustness analysis on the model performance under supportive data featuring good and poor quality, it is confirmed that the probabilistic joint inversion procedure approximates the fracture geometry and aperture well, and errors in predicting temperatures based on realizations of fracture networks are well below 5%. The methodology provides a new way to characterize fracture networks in the subsurface, without restrictions on predetermined fracture sizes or the number of fractures.

Plain Language Summary Mapping the fracture geometry explicitly is a crucial step toward the realistic prediction and management of flow and transport reservoirs. However, the determination of fracture geometry to a high resolution in the subsurface is still an unsolved problem in geoscience. This study presents a novel joint inversion framework enabling high-resolution fracture network imaging by fusing the microseismic data and thermal tracer test data. Both datasets are widely available in reservoirs such as enhanced geothermal systems and shale gas/oil reservoirs. The performance of the new model in characterizing the fracture profiles is evaluated, and the results demonstrate that the model provides a computationally efficient and high-accuracy way for fracture network imaging in deep reservoirs.

1. Introduction

In fractured rock reservoirs, often considerable permeability contrasts exist between a dense rock matrix and open intersecting fractures. Flow and fast transport are focused in a network of hydraulically connected fractures with unique characteristics that depend on diverse processes governing rock formation and deformation. Accordingly, reliable characterization of fractures in the field is counted among the most difficult problems in hydrogeology (Berkowitz, 2002; Neuman, 2005). When reproduced in groundwater or other reservoir models, fractured reservoirs are commonly described by either a continuum approach or by a discrete fracture network (DFN). The former smoothens the fracture network as a highly heterogeneous porous medium and expresses hydraulic properties of fractures as upscaled permeability tensors (Day-Lewis et al., 2000; Illman et al., 2009), while the latter explicitly delineates fracture geometry and apertures (Afshari Moein et al., 2018; Maillot et al., 2016; Nejadi et al., 2017).

Continuum models are appealing due to their computational efficiency, and the spatial permeability distribution can be estimated by established model calibration procedures. In particular, this has been demonstrated

© 2023. American Geophysical Union. All Rights Reserved.

JIANG ET AL. 1 of 22 by processing cross-well pressure, solute concentration or temperature responses with inversion algorithms in hydraulic and tracer tomography applications (Brauchler et al., 2013; Illman et al., 2009; Liu et al., 2022; Schöniger et al., 2012; Tiedeman & Barrash, 2020; Zha et al., 2015; Zhao et al., 2021). Such continuum models are especially suited for representing the conditions in dense networks with many interconnections among the fractures. However, inherent smoothing of sharp contrasts may overestimate the permeability of a rock matrix and underestimate the permeability of fractures, and thus flow focused in sparse fractures is not well represented (Dong et al., 2019; Long et al., 1982). Here, mapping the fracture geometry by a DFN model explicitly is favorable, as it allows for a more realistic tracking of preferential flow and transport paths in a reservoir (De Dreuzy et al., 2012; Hyman et al., 2019; Klepikova et al., 2020). In reservoirs of enhanced geothermal systems, for example, resolution of hydraulically active fractures can provide a crucial insight in the in-situ heat exchange mechanisms, the effective contact surface between fluid and matrix, and ultimately the efficiency and lifetime of a geothermal plant.

DFNs can be generated stochastically, subject to probability distributions of fracture lengths and orientations. These distributions are derived for instance by mapping fracture geometry from two-dimensional (2D) outcrop planes or by analyzing one-dimensional (1D) borehole lines (Vidal et al., 2017). A common assumption is that the fracture length distribution follows a power law (Marrett et al., 1999), and fracture patterns at different scales feature apparent similarity (Tchalenko, 1970). To represent a three-dimensional (3D) fracture network based on 1D and 2D fracture measurements, the power law expressing fracture sizes at multiple scales is complemented ideally by stereological analysis (Darcel et al., 2003). These concepts enable the generation of stochastic fracture networks at regional scales based on local-scale observations.

In practice, sufficient field data rarely exist to arrive at one reliable deterministic model of spatial fracture characteristics. Therefore, inversion models have been refined to better constrain the fracture geometry by parameter dimensionality reduction (Jiang et al., 2021; Vu & Jardani, 2022). In order to constrain stochastic DFN representations, conceptual assumptions, and soft knowledge (including such as geophysical and hydraulic responses to fracture geometry) need to be combined with smart mathematical inversion of high-resolution measurements and, ideally, different types of complementary data. For example, hydrogeophysical inversion concepts are available that augment hydraulic and tracer data with geophysical information, such as from ground penetration radar surveys (Dorn et al., 2013) or electrical resistivity imaging (Farooq et al., 2022). The surface deformation monitoring with tiltmeters are combined with periodic hydraulic tests to infer mechanical properties of fractured reservoirs (Schuite et al., 2017). Aside from these, seismicity interpretation can provide promising information to reveal the structures in deep reservoirs (Lehujeur et al., 2018). In enhanced geothermal systems and unconventional gas/oil reservoirs, valuable knowledge often exists about locations, magnitudes and focal mechanisms of microseismic (MS) events induced by hydraulic stimulation or fracturing (e.g., Folesky et al., 2016; Majer et al., 2007; Maxwell, 2014; Shapiro et al., 2006). The spatiotemporal distribution of MS events is related to the propagation of fractures in a reservoir (Fadakar Alghalandis et al., 2013; McKean et al., 2019; Wang et al., 2013; Williams-Stroud et al., 2013), but the relationship between microseismicity and fracture geometry is still in debate (Cornet, 2000; Cornet et al., 2007; Shapiro et al., 1999). MS events often result from deformations directly induced by hydraulic fracturing, which are referred to as "wet" events. The geometry of hydraulically active fractures, that is, the target of this study, can be located according to the positions of wet MS events. However, stress and pressure changes at positions away from hydraulic fractures also induce "dry" MS events due to slip on existing fractures. The inclusion of dry events could lead to the overestimation of hydraulic fracture geometry, which should be excluded by the diagnostic analysis based on the relationship between the occurrence time of MS events and distances to the fracturing well, or between the frequency and magnitude of MS signals. Moreover, it is documented that the majority of energy input during hydraulic fracturing is consumed in aseismic tensile deformation and fluid friction (Maxwell et al., 2008, 2015a). MS events that occur with shear deformation and at the tip of tensile fractures are not indicative for fracture apertures. MS properties form 3D information to reconstruct fracture network geometry (Aminzadeh et al., 2013), despite them providing limited insight in the hydraulic connectivity of the fracture network. Better capturing the hydraulic connectivity is necessary for the reduction of the uncertainty in fracture network characterization.

In order to capture their hydraulic connectivity and enhance capability to predict flow and transport, fracture networks are most efficiently constrained by pressure and tracer signals recorded at multiple sources and receivers during tomographic cross-well testing. Somogyvári et al. (2017) introduced a transdimensional inversion algorithm, which is also referred to as the reversible jump Markov chain Monte Carlo (rjMCMC), to generate

JIANG ET AL. 2 of 22

2D fracture networks based on these tomographic tests. The inversion procedure was successfully employed for tracer and hydraulic tomography (Ringel et al., 2019), and it was advanced for 3D fracture network imaging (Ringel et al., 2021) including stochastic representation of DFNs by fracture probability maps.

This study builds on the 2D rjMCMC framework by Somogyvári et al. (2017) and enhances heat tracer data inversion by MS data. Heat is chosen as a tracer to represent conditions in enhanced geothermal systems and unconventional gas/oil reservoirs, where MS events are detected during reservoir hydraulic fracturing by pressurization, and thermal breakthrough curves are obtained during trial-production testing. The objective thus is to introduce a stochastic DFN identification concept that utilizes synergies of thermal tracer tomography and MS data. The underlying rationale is that these complementary information sources can enhance the convergence of the stochastic inversion procedure in comparison to applying thermal tracer tomography alone. Moreover, a better resolution of the fracture probability is expected, thereby reducing the uncertainty of the results. This is especially the case for inversion problems in deep reservoirs with a limited number of boreholes for well tests data acquisition and geophysical data containing significant measurement uncertainties. In the following, two test cases of 2D sections of geothermal reservoirs featuring synthetic simple fracture patterns and realistic fracture patterns are set up for applying the new inversion procedure.

2. Methodology

The methodology orients the available data in deep reservoirs in practice. Such data and knowledge include an expected minimum number of fractures and characteristic fracture orientations revealed by borehole imaging. At field sites, trial production test via doublet wells may provide thermal breakthrough curves, and often clouds of MS events induced by reservoir stimulation are recorded. In order to integrate this information for DFN characterization, a joint MS and thermal data inversion framework is proposed through the following steps: (a) prior parameters sampling from the known probability distributions indicated by optical or acoustic borehole logs, (b) proposal fracture network generation from MS data based on the prior parameters, (c) forward flow and heat transport modeling to calculate the thermal breakthrough curve, and (d) fracture network evaluation and updating based on the misfit between calculated and observed thermal breakthrough data, following Bayes' theorem (Figure 1).

2.1. Prior Information on Fracture Network

The prior knowledge required for the inversion procedure includes a minimum number of fractures, probability distributions of fracture orientations and fracture apertures (Figure 1a). The minimum number of fractures (n_{min}) can be defined as the number of fractures revealed by boreholes, where $n_f \sim UI(n_{min}, \infty)$ with n_f indicating fracture number and UI representing a random integer featuring the uniform distribution. The orientation of fractures often features two (or more) conjugate fracture sets (e.g., Valley, 2007; Ziegler et al., 2015); for each set, the fracture orientations (s) follow the uniform probability distribution, that is, $s \sim U(s_{min}, s_{max})$, where U represents the uniform distribution, s_{min} and s_{max} represent the minimum and maximum orientation, respectively, defined according to downhole imaging.

Fractures detected at the borehole wall often include drilling-induced tensile fractures in addition to fractures originally existing in the reservoir. The drilling-induced fracture is indicative for the in-situ stress regime. Thus, orientations of drilling-induced fractures and original fractures provide critical information indicating orientations of hydraulic-active fractures induced by pressuring the reservoir (Afshari Moein et al., 2018). However, drilling-induced fractures often occur at shallow depth near the borehole wall. Including drilling-induced fractures in the minimum number of fractures thus could lead to the overestimation of the number of hydraulically active fractures. It is thus necessary to distinguish drilling-induced fractures and original fractures (Brudy & Zoback, 1999; Zoback et al., 2003), and to employ the number of original fractures as the minimum estimations on the fracture number (n_{min}).

Moreover, the fracture (hydraulic) aperture (b) is assumed to follow a uniform logarithm distribution, with values of 10^{-4} to 10^{-2} m according to those reported in enhanced geothermal reservoirs (e.g., AbuAisha et al., 2016; Bruel, 2002; Wu et al., 2021). It is noted that fracture apertures measured at the borehole walls are not suggested to be used for the prior distribution on hydraulic apertures, since they often deviate from hydraulic fracture apertures in reservoirs, due to mud clogging and uneven distributions of hydraulic pressures and in-situ stress regime.

JIANG ET AL. 3 of 22

19447973, 2023, 9, Downloaded from https://agupubs.onlinelibrary.wiley.com/doi/10.1029/2022WR034339 by Eth Zürich Eth-Bibliothek, Wiley Online Library on [07/09/2023]. See the Terms

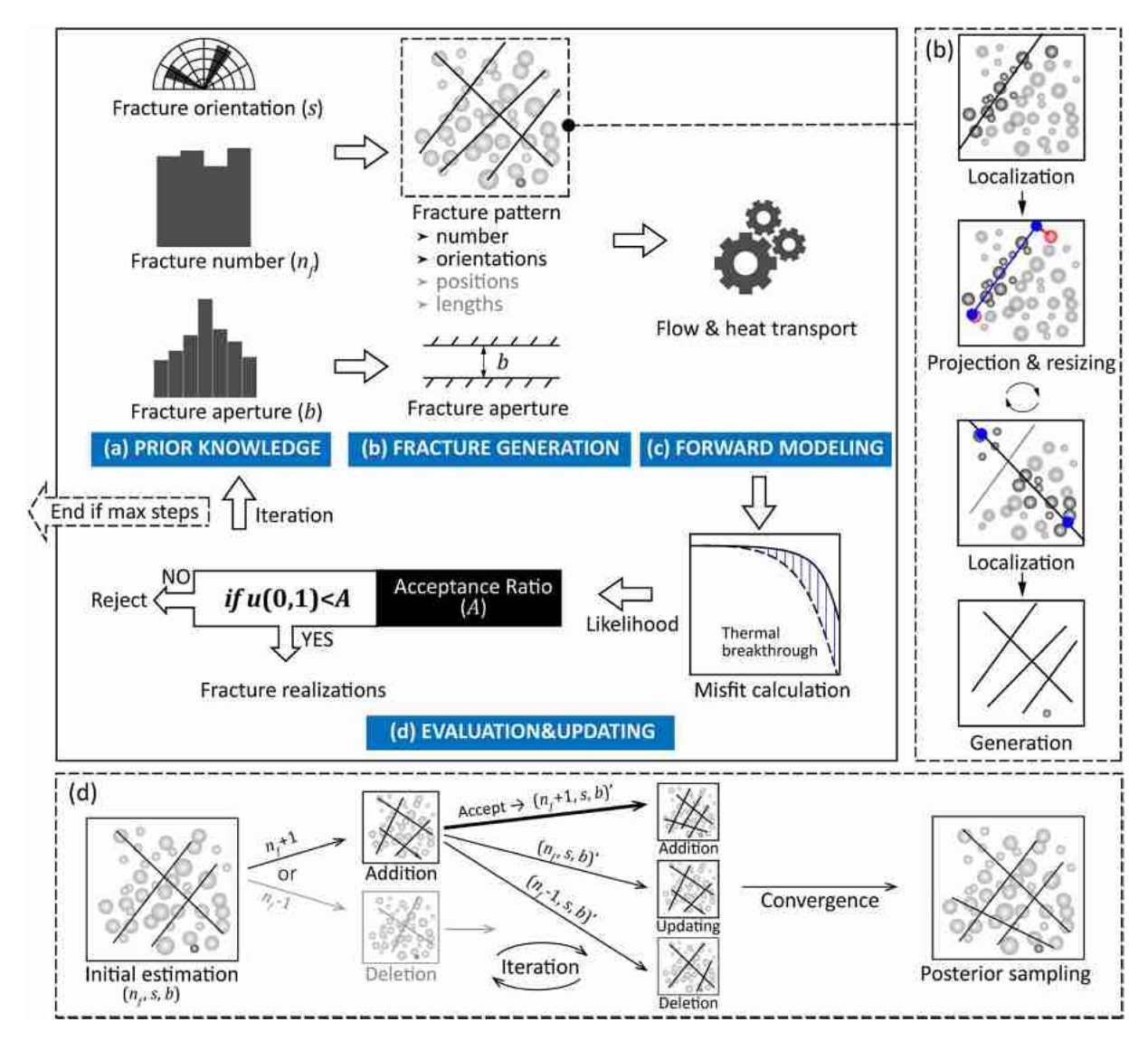


Figure 1. Framework for the fracture network characterization by joint microseismicity (MS) and thermal breakthrough data inversion, including (a) prior parameter sampling from information revealed by boreholes, (b) fracture network generation from MS data, (c) forward flow and heat transport modeling, (d) evaluation and updating according to Metropolis-Hastings-Green criteria.

Other prior probability distributions rather than the uniform priors for fracture orientations, apertures and number are also applicable in the proposed inversion algorithm framework, depending on the probability distribution indicated by borehole logs and outcrop survey in a specific site.

2.2. Fracture Network Generation Based on MS

MS events are induced by pressurizing a subsurface rock formation. For the purpose of characterizing the final-state fracture network after hydraulic fracturing, it is assumed that the employed MS events are pre-processed to exclude dry events by typically density-based spatial clustering of applications with noise and focal mechanism analysis (Maxwell, Mack, et al., 2015). The model in this study starts from the processed MS events, that is, wet events occurred at shear fractures and tips of tensile fractures are collected to form one MS events cloud. These events theoretically lie on hydraulically activated fractures, although errors always occur in the localization of MS events due to limitations in monitoring techniques and interpretation algorithms. Once the positions of wet

JIANG ET AL. 4 of 22

MS events have been interpreted in a fractured reservoir, fracture networks can be generated to reduce the average distance of MS events to fractures. The target function $(L_e(m))$ is defined as:

$$L_{s} = \frac{\sum_{i=1}^{n_{f}} \sum_{j=1}^{p} \|d_{i,j}\|}{n_{f} p_{f}},$$
(1)

where n_f is the number of fractures, p is the number of MS events, p_f is the number of MS events included by the fractures. $d_{i,j}$ (m) is the Eulerian distance of the jth MS event to the ith fracture. The smaller L_s is, the better the fit is between fracture and MS events.

Based on the prior estimations on fracture number (n_f) and orientations, a fracture network is generated from MS events by the following steps (Figure 1b):

Localization: An MS event is randomly selected from the MS cloud, which is used as the reference position of a fracture. The orientation of this fracture is sampled from the prior probability distribution of orientations. In this stage, the sampled fracture features infinite size. The distances of all localized MS events to this fracture are calculated, and MS events included by this fracture are identified as those with distances lower than the tolerance given as the maximum error in the localization of MS events.

Projection and resizing: The included MS events are projected on this fracture, and the minimum and maximum coordinates of MS events after the projection are recorded to estimate the size of the fracture (*l*). For the 2D fracture network characterization, the length of the fracture is estimated by:

$$l = \sqrt{(x_{max} - x_{min})^2 + (y_{max} - y_{min})^2},$$
(2)

where x_{max} (m) and x_{min} (m) represent the maximum and minimum coordinates in x direction, respectively, and y_{max} (m) and y_{min} (m) represent those in y direction, respectively. The coordinates (position) of the fracture center (x_c, y_c) are defined as:

$$\mathbf{x} = (x_c, y_c) = \left(\frac{x_{max} - x_{min}}{2}, \frac{y_{max} - y_{min}}{2}\right)$$
(3)

The included MS events are then removed from the MS cloud, for which the localization, projection and resizing steps above are repeated until the number of fractures is equal to n_f .

Generation: Repeating the steps above generates one fracture network, defining fracture orientations, sizes and center positions of each fracture, based on the prior estimation on fracture number and fracture orientations, and the spatial distribution of MS events.

Moreover, the aperture (b) sampled from the prior uniform probability distribution is defined for each fracture, leading to a DFN model. The reliability of the model is evaluated by the misfit between an observed and simulated thermal breakthrough curve (Figure 1c).

2.3. Forward Modeling of Flow and Heat Transport

The embedded discrete fracture model (EDFM) that treats fracture and matrix as two separate computational domains is employed in this study. The model enables calculating flow and heat transport efficiently (Hajibeygi et al., 2011; Jansen et al., 2018). In the EDFM, the governing equations for steady-state fluid flow in the fracture and matrix are expressed as:

$$\nabla \left[\frac{k^m}{\mu^m} (\nabla p^m - \rho_f g) \right] + \Psi^{mf} = 0, \tag{4}$$

$$\nabla \left[\frac{b^2}{12\mu^f} \left(\nabla p^f - \rho_f g \right) \right] + \Psi^{fm} + Q = 0, \tag{5}$$

where k is the permeability (m²), μ is the fluid viscosity (Pa·s), p is the fluid pressure (Pa), Ψ is flux transfer functions between matrix and fracture (s⁻¹), b is the hydraulic aperture (m), and Q is the source or sink of fluid

JIANG ET AL. 5 of 22

(s⁻¹), ρ is the fluid density (kg·m⁻³), g is the gravity acceleration (m·s⁻²), and the superscript m and f represent the matrix and fracture, respectively.

The transient heat transport in matrix and fracture is namely governed by:

$$\widetilde{c}\widetilde{\rho}^m \frac{\partial T^m}{\partial t} + (c_f \rho_f u^m) \nabla T^m - \lambda^m \nabla^2 T^m = \chi^{mf}, \tag{6}$$

$$\widetilde{c}\rho^f \frac{\partial T^f}{\partial t} + \left(c_f \rho_f u^f\right) \nabla T^f - \lambda^f \nabla^2 T^f = q^f + \chi^{fm},\tag{7}$$

where $\tilde{c}\rho$ is the averaged heat capacity of both rock matrix and fluid (J·m⁻³ °C⁻¹), $c_f\rho_f$ is the heat capacity of a fluid (J·m⁻³ °C⁻¹), T is temperature (°C), λ is the thermal conductivity (W·m⁻¹ °C⁻¹), χ represents the heat exchange between matrix and fracture (W·m⁻³), q^f is the heat source along with the fluid injection (W·m⁻³), and u represents the fluid velocity defined as:

$$u = -\frac{k}{\mu}(\nabla p - \rho_f g),\tag{8}$$

Considering the computational efficiency, this study focuses on the model development and verification based on 2D fracture networks, where Equations 4–8 are solved sequentially by the explicitly finite different method with the open-source codes, THERMAID (Jansen et al., 2018). First, the governing equations for the steady-state fluid flow in matrix and fracture are solved, resulting in the spatial distribution of velocity. The flow velocity is then employed in the advection-dispersion equations (Equations 6 and 7), resulting in outflow temperatures at extraction position(s).

In this study, coupling with mechanical effects is not considered since the model is developed to characterize the final state of a fracture network after reservoir stimulation. The influences of temperature and pressure on fluid density and viscosity are neglected, and the effects will be discussed further.

The misfit (L_t) between calculated outflow temperatures and observations is expressed as:

$$L_t = \frac{1}{N} \sum_{i=1}^{N} \left(\frac{T_i^{obs} - F_i(n_f, s, b)}{\sigma} \right)^2 \tag{9}$$

where N is the number of temperature observations, T^{obs} is the observed temperature, σ is the standard deviation of measurement errors (following a zero-mean normal distribution), $F(n_ps,b)$ represents the calculated outflow temperature via forward model of flow and heat transport (Equations 4–8) given a fracture network generated from MS events including fracture number (n_f) , orientations (s) and aperture (b). The values of n_ps and b are iteratively updated to characterize the posterior estimations of the fracture network based on a transdimensional inversion rule. This means, the MS information is used to fix potential central fracture positions and sizes, whereas the following inversion decides upon their individual existence, orientation and aperture.

2.4. Inversion Procedure

Since flexible adjustment of the DFN requires the variation of the fracture number (i.e., the dimensionality of parameters), the rjMCMC method is employed, which is especially suited for dealing with a problem featuring an unknown number of parameters (Green, 1995) (Figure 1d).

In Bayes' theorem, the posterior probability of fracture parameters, $p(\theta | T_{obs})$, can be rewritten as:

$$p(\theta|T_{obs}) \propto p(\theta)p(T_{obs}|\theta).$$
 (10)

where $p(\theta)$ represents the prior probability of fracture parameters and $p(T_{obs}|\theta)$ represents the likelihood. A full list of parameters characterizing the fracture network is expressed as $\theta = \{n_p, s, x, l, b\}$. Among these parameters,

JIANG ET AL. 6 of 22

 n_p s, b are updated by the inversion, while fracture center positions x and l have been inferred from MS events based on the algorithm described in Section 2.2. Thus, Equation 10 can be simplified as:

$$p(n_f, s, b|T_{obs}) \propto p(n_f, s, b)p(T_{obs}|n_f, s, b). \tag{11}$$

The prior probability $p(n_f, s, b) = p(n_f)p(s)p(b)$, whereby n_f , s and b are sampled independently from the predefined uniform prior distributions. $p(T_{obs}|n_f, s, b)$, signifies the likelihood function of n_f , s, and b. For convenience, the logarithm of the likelihood function is employed:

$$p(n_f, s, b|T_{obs}) = -\frac{N}{2}\log(2\pi) - N\log\sigma - \frac{N}{2}L_t$$
 (12)

The acceptance or rejection of fracture parameters is evaluated by the Metropolis Hastings Green (MHG) criterion, $A(\mathbf{r}, \mathbf{r}')$ (Green, 1995):

$$A(\mathbf{r}, \mathbf{r}') = \min \left\{ 1, \frac{\pi(\mathbf{r}')}{\pi(\mathbf{r})} \cdot \frac{q(\mathbf{r}|\mathbf{r}')}{q(\mathbf{r}'|\mathbf{r})} \cdot \left| \frac{\partial \mathbf{r}'}{\partial \mathbf{r}} \right| \right\},\tag{13}$$

where r and r' indicate the present and new states of the subset of fracture parameters (n_f, s, b) to be updated in the inversion, respectively, π represents the posterior probability of fracture parameters (Equation 11). The identical probability distribution for prior parameters is assumed in each iteration, thus,

$$\frac{\pi(\mathbf{r}')}{\pi(\mathbf{r})} = \frac{p(\mathbf{r}'|T_{obs})}{p(\mathbf{r}|T_{obs})}.$$
(14)

 $\frac{q(r|r')}{q(r'|r)}$ represents the proposal probability for generating new-state parameters. Three different types of perturbations to generate fracture parameters are employed, including (a) the "update" step that maintains fracture geometry unchanged and perturbs only the aperture, (b) the "addition" step that increases the fracture number to $n_f + 1$ from the present state featuring n_f fractures, and regenerates the fracture network from MS event (Section 2.2), and (c) the "deletion" step that decreases the fracture number to $n_f - 1$ and regenerates the fractures (Figure 1d).

Initially, random fracture parameters of (n_p, s, b) are sampled from their priors to generate a DFN and calculate the likelihood and posterior. This is followed by the addition or deletion operations randomly selected with an equal probability of 1/2. Once the operation is accepted, it obtains a higher probability (ε_p) sampled from the uniform distribution of (0.5, 1.0), to compare with a random variable ε_1 sampled from the uniform distribution of (0.0, 1.0). If ε_p is larger than ε_1 , this operation maintains in the next step. Otherwise, the other two operations are selected with an equal probability of 1/2. Once the operation is rejected, three possible operations are randomly selected with an equal probability of 1/3 in the next step. For each type of operation, the proposal probability ratio is defined below.

(1) *Update:* Fracture aperture of new state is perturbed by a random variable Δb sampled from the standard normal distribution, that is, $b' = b + \Delta b$. The fracture geometry maintains unchanged. The proposal probability function is written as:

$$q(\mathbf{r}'|\mathbf{r}) = q(b'|b) = \frac{1}{\sqrt{2\pi}} \exp\left[-\frac{(b'-b)^2}{2}\right]. \tag{15}$$

The probability of generating a perturbed b' from present state of b is the same as the reverse probability of generating b from the state of b'. Thus,

$$\left[\frac{q(\mathbf{r}|\mathbf{r}')}{q(\mathbf{r}'|\mathbf{r})}\right]_{update} = 1.$$
 (16)

(2) Addition: For an addition step, parameters \mathbf{r} for n_f fractures jump to \mathbf{r}' for $n_f + 1$ fractures. This step involves the regeneration of fracture network geometry from MS events and fracture aperture resampling for

JIANG ET AL. 7 of 22

one more fracture. Fracture aperture b is independent of the parameters $(n_p s)$ defining the fracture geometry, the proposal probability function is rewritten as:

$$\frac{q(\mathbf{r}|\mathbf{r}')}{q(\mathbf{r}'|\mathbf{r})} = \frac{q(n_f, s|\mathbf{r}')q(b|\mathbf{r}')}{q(n_{f'}, s'|\mathbf{r})q(b'|\mathbf{r})}.$$
(17)

Parameters (n_f', s') lead to a fracture network based on MS events, $q(n_f', s'|\mathbf{r})$ is defined by:

$$q(n_f', s'|\mathbf{r}) = \exp(|L_{s'}|^2), \tag{18}$$

where L_s' is the average distance between fractures and MS events (Equation 1), corresponding to the new state of n_f' , s'. Additionally, $q(b'|\mathbf{r})$ in response to the addition of a fracture is expressed as:

$$q(b'|\mathbf{r}) = \frac{1}{\log(b_{max}) - \log(b_{min})}.$$
(19)

Furthermore, $q(n_f, s | r')$ for the reverse operation is defined as:

$$q(n_f, s|\mathbf{r}') = \exp(|L_s|^2). \tag{20}$$

$$q(b|\mathbf{r}') = 1. (21)$$

Substituting Eqs. (18)–(21) into (17), leads to

$$\left[\frac{q(\mathbf{r}|\mathbf{r}')}{q(\mathbf{r}'|\mathbf{r})}\right]_{addition} = \frac{\log(b_{max}) - \log(b_{min})}{\exp(|L_s'|^2 - |L_s|^2)}.$$
 (22)

The rationale for Eq. (22) is that the lower misfit between new state of fractures and MS events (L_s') corresponds to a higher proposal probability ratio, and thus higher $A(\mathbf{r}, \mathbf{r}')$.

(3) *Deletion:* In a deletion step, $q(b'|\mathbf{r}) = 1$, $q(b|\mathbf{r}') = [\log(b_{max}) - \log(b_{min})]^{-1}$, and $q(n_f', s'|\mathbf{r})$ and $q(n_f, s|\mathbf{r}')$ is expressed by Eqs. (18) and (20), respectively, the proposal probability ratio is expressed as:

$$\left[\frac{q(\mathbf{r}|\mathbf{r}')}{q(\mathbf{r}'|\mathbf{r})}\right]_{deletion} = \frac{\exp\left(|L_s|^2 - |L_s'|^2\right)}{\log(b_{max}) - \log(b_{min})}.$$
 (23)

The last term $\left|\frac{\partial r'}{\partial r}\right|$ in Equation 13 represents the Jacobian matrix, which is equal to 1.0 in this study since the addition and deletion of fractures lead to the variation of parameters independent of the parameters of other fractures.

Once $A(\mathbf{r},\mathbf{r}')$ is determined in each step during the inversion, a random number (ε_2) is drawn from 0 to 1 following the uniform distribution. The new state of fracture parameters is rejected if $A < \varepsilon_2$; otherwise, the proposed state of parameters is accepted and stored. The stored set of DFN configurations represents the result of the inversion.

A sufficient number of iterations is required in the rjMCMC algorithm, in order to better characterize the posterior distribution of fracture parameters. The first few hundreds to thousands of iterations are referred to as the burn-in period, when the misfit between calculated and observed temperatures rapidly reduces to the measurement error of the outflow temperatures. Subsequently, the misfit fluctuates around a stable value, indicating the convergence of the inversion and providing feasible DFN realizations that can be evaluated as the inversion result.

3. Test Cases

Two 2D examples are set up to assess the effectiveness of the proposed inversion algorithm. One example is simply composed of four fractures, which is employed to directly evaluate the accuracy of the inversion model in characterizing the fracture number, orientation, position, length and aperture. Another example is composed

JIANG ET AL. 8 of 22

-1500

-1520 £-1540

-1560

-1580

-1600

-1500

-1520

€-1540

-1560

-1580

(a)

300

300

(d)

200

Temperature at 5 days

150

200

19447973, 2023, 9, Downloaded from https://agupubs.onlinelibrary.wiley.com/doi/10.1029/2022WR034339 by Eth Zürich Eth-Bibliothek, Wiley Online Library on [07/09/2023]

-1500

-1520

-1580

-1600

-1500

-1520

-1560

-1580

-1600

€ -1540

 Injection position Extraction/Observation

> 100 150

50

Depth

Figure 2. (a) Synthetic fracture network composed of four fractures, (b) microseismic events in response to the fracture network with localization errors ranging in ±10 m, (c) thermal breakthrough curves during a trial-production test, and (d)–(f) illustrating the spatial distribution of temperatures at 5, 10, and 30 days, respectively.

150 200

150

emperature at 10 days

200

100

of 17 fractures extracted from realistic outcrop field data, which is used to assess the capability of the inversion model in capturing the fracture skeleton and in predicting the outflow temperature under alternative injection and extraction scenarios.

(b)

(e)

250

3.1. Simple Case

This case simulates a 2D profile in a geothermal reservoir at depth ranging from 1,500 m to 1,600 m. The width of the reservoir and fractures perpendicular to the 2D profile is assumed to be unity. Four fractures are set at the reservoir: three of them intersect boreholes, that is, orientations and relative positions of these fractures are determined with unknown fracture lengths and center positions; another fracture is not revealed by boreholes, which is hereafter referred to as the hidden fracture (Figure 2a). Two approximately conjugated fracture orientations are defined at 10° and -20° , respectively, with the reference angle at the horizontal and right direction as zero. It is assumed that the stimulation of these hydraulic active fractures by pressuring the geothermal reservoir leads to over 1,000 MS events. For a realistic setup of the test case, noise in a range of ±10 m following the uniform probability distribution is added to the cloud of MS events (Figure 2b).

The initial pressure in the model domain is given at 20 MPa, and the initial temperature is 100°C. Any pressure and temperature gradients in the vertical direction are neglected. The left and right boundaries of the 2D flow and heat transport model are specified by a constant pressure of 20 MPa. At the upper and lower end, the model is delimited by a zero-flux boundary. Moreover, temperatures at all surrounding boundaries are set fixed at 100°C.

A trial-production test of 30 days is conducted by injecting relatively cold water with a temperature of 50°C at the injection well. The permeability of the matrix is assumed to be extremely low, with a value of 10^{-20} m². The thermal conductivity of the rock matrix is given at 2.0 W·(m·°C)⁻¹. A uniform aperture of 0.001 m is defined at each fracture. An injection rate of 3 kg·s⁻¹ is assumed at the intersection of the fracture and injection well. Similarly, an extraction rate of 1 kg·s⁻¹ is defined at three intersections of fracture and extraction well, respectively (Figure 2a). The injection rate is equilibrium to the total extraction rate. Outflow temperatures are monitored at three intersections of the fracture and the extraction well (Figure 2a), separately. It is illustrated that for the given fracture network that the earliest cool water breakthrough occurs at observation position 2, followed by positions 4 and 3, respectively (Figures 2d-2f). The fast water flow along the flow path from the injection position to position 2 leads to a short time for fracture-matrix heat exchange. Thus, low outflow temperature occurs. In contrast, the highest outflow temperatures are observed at position 3 (Figure 2c). In order to mimic the errors occurring in

JIANG ET AL. 9 of 22

19447973, 2023, 9, Downloaded from https://agupubs.onlinelibrary.wiley.com/doi/10.1029/2022WR034339 by Eth Zürich Eth-Bibliothek, Wiley Online Library on [07/09/2023]. See

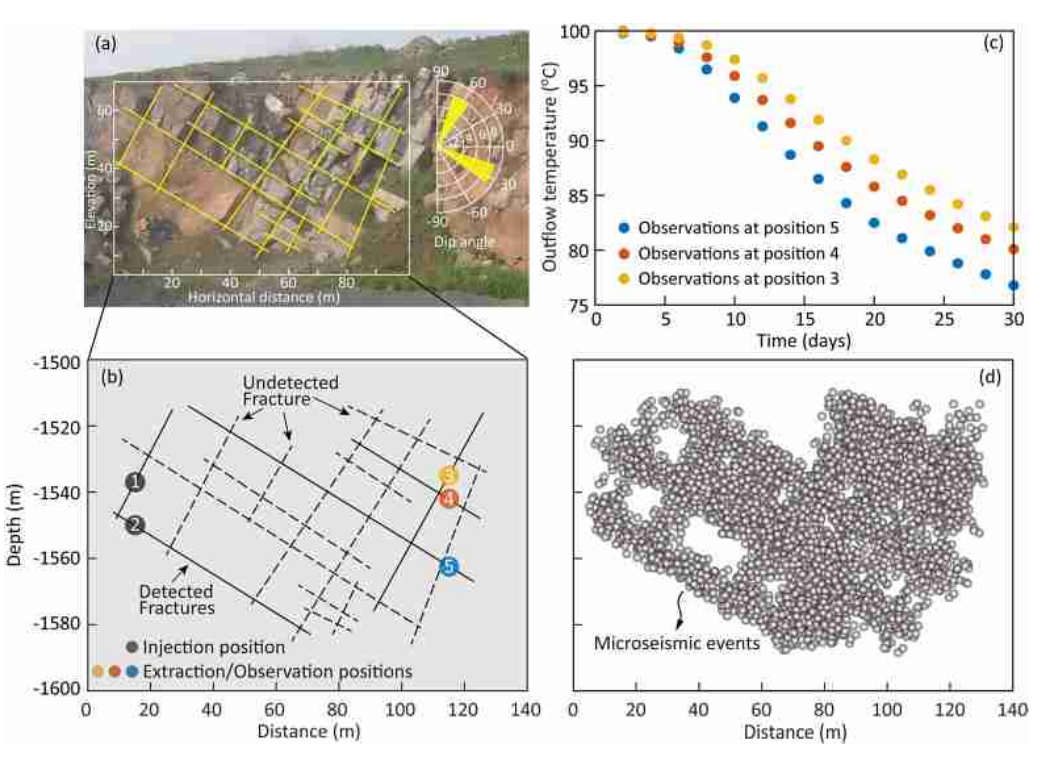


Figure 3. (a) Synthetic fracture network composed of 17 fractures extracted from a field outcrop, which is assumed to be buried at depth of 1,500 m to 1,600 m, forming a fractured geothermal reservoir (b). (c) Thermal breakthrough curves monitored at positions 3 to 5 during the trial-production test and (d) the spatial distribution of microseismic events induced by pressuring the reservoir.

realistic observations, random noises following a zero-mean normal distribution with the standard deviation of 1.0° C are assigned to outflow temperatures, yielding three temperature breakthrough curves with a measurement error of 1.0° C (Figure 2c).

Conditional to thermal breakthrough curves and MS events, fracture networks are generated by the rjMCMC inversion algorithm. Boundary conditions for fluid and heat transport are fixed during the inversion. The prior fracture orientation is presumed to range from 0° to 20° and -10° to -30° , respectively, following a uniform distribution, representing the potential variation on the orientation of hidden fractures in comparison to those revealed by downhole logs. The fracture aperture is assumed to range from 10^{-4} to 10^{-2} m, representing a general range of fracture aperture in the reservoir. The minimum number of fractures is set to a value of three, representing the number of fractures revealed by downhole logs. No prior knowledge on the maximum number of fractures is required. Prior knowledge on lengths and positions of fractures is also not defined, as both are evaluated from MS events.

3.2. Outcrop-Based Case

A more complicated fractured reservoir is designed according to the fracture pattern taken from an outcrop profile in the Gonghe Basin, China (Figure 3a). The DFN is composed of 17 fractures. Five fractures are revealed by downhole logs and the other 12 fractures are hidden. These fractures are assumed to be buried in the subsurface at a depth of 1,500 m to 1,600 m, forming a fracture reservoir (Figure 3b). It is assumed that the stimulation of these fractures leads to 4,000 MS events (Figure 3d).

According to the temperature and pressure conditions in the geothermal reservoir in the Gonghe Basin (Zhang et al., 2021), the initial temperature and pressure in this model is given at 100°C and 20 MPa, respectively. The lateral model boundary conditions are given as those in the previous simple case. The aperture of fractures is assumed to be 0.001 m. During a trial-production test of 30 days, cool water is injected into the reservoir via the injection well at positions 1 and 2 (Figure 3b), under a constant rate of 2 kg·s⁻¹. Warm water is extracted via the

JIANG ET AL. 10 of 22

The fracture network is then characterized by the rjMCMC inversion procedure, where the minimum number of fractures is defined at five, the prior orientation of fractures ranges from 55° to 70° and -25° to -35° , according to the downhole logs at positions 1 to 5 (Figure 3a). The prior aperture is assumed to range from 10^{-4} to 10^{-2} m following a logarithm uniform distribution.

3.3. Performance Metrics

3.3.1. Convergence Diagnostic

The rjMCMC performs the non-continuous updating on fracture parameters to minimize the misfit between calculations and observations. The convergence diagnostic employed in the classical MCMC algorithm is often not directly applicable for the transdimensional inversion (Bodin & Sambridge, 2009). In this study, the model convergence is firstly judged by the misfit (*RMSE*, Equation 24) between calculated and observed temperatures below the measurement error.

$$RMSE = \sqrt{\frac{1}{N} \sum_{i=1}^{N} (T_i^{obs} - T_i^{cal})^2},$$
 (24)

where T^{obs} and T^{cal} represent the observed and calculated temperatures, respectively. Subsequently, the inversion procedure is repeated by 500, 1,000, 2,000 iterations or more. If the *RMSE* shows negligible changes during ongoing iteration, the posterior distribution of fractures is considered to be sufficiently sampled and the iteration can be terminated. Otherwise, the iteration should be continued (Somogyvári et al., 2017).

3.3.2. Reliability of the Inversion Model

In the simple case with four fractures, three fractures are intersected by boreholes, where the relative positions and orientations are assumed to be known. One hidden fracture is left to be delineated explicitly by the inversion model. The generated fracture network can be directly compared to the true model, and the model accuracy is quantified by the absolute errors in the fracture number, and the center position, length, orientation, and aperture of the hidden fracture.

For the more complex fracture network of the outcrop-based case, it is difficult to directly compare the generated fracture geometry with the true ones. A qualitative criterion is to visually compare the true fracture network with the probability map of fracture realizations, which is defined as the frequency of fracture occurrence at each pixel after rasterizing the maps of fracture realizations. Furthermore, in order to quantitatively evaluate the reliability of generated fracture networks, an independent trial-production test is simulated by alternative injection and extraction rates at different positions, in comparison to the conditions employed to generate breakthrough curves for fracture network inversion. In the outcrop-based case, cool water is injected at position 2 and extracted at position 5, under a constant rate of 2 kg·s⁻¹ for 30 days (Figure 3b). As a result, another thermal breakthrough curve is generated for model validation (Figure 10c). The misfit (*RMSE*) of calculated and observed outflow temperatures in response to each realization of the fracture network is employed as the criterion to examine if the generated fracture network is reliable and capable to predict the thermal performance (Wu et al., 2021). The thermal breakthrough curves employed for fracture network inversion are referred to as the "inversion dataset", and those employed for fracture network validation are referred to as the "validation dataset".

4. Results and Discussion

4.1. Simple Case

4.1.1. Sensitivity Analysis

In order to assure that the fracture parameters can be inferred from tracer breakthrough curves, the sensitivity of the outflow temperatures at the three observation positions to different parameters of the fracture network is analyzed. In the following, the parameters employed in the synthetic fracture network in Section 3.1 (Figure 2)

JIANG ET AL. 11 of 22



are considered as the base case; the sensitivity analysis is conducted by varying the parameters of the hidden fracture (number of fractures, position, length, orientation and aperture) while keeping the other parameters of the DFN constant.

It is illustrated that altering the number of fractures from three to 10, the outflow temperatures at observation positions 2 and 3 are highly affected, with the temperature at the 30th day varied by over 20°C (Figure 4a). In this study, constant rates are defined at both injection and extraction positions. The more hidden fractures, the more flow pathways are possible between injection and extraction positions, thus, the lower the flow velocity. This leads to a longer interaction time for the fracture-matrix heat exchange; consequently, the outflow temperature at observation positions 2 and 3 increases with the number of hidden fractures. With the decrease of the flow velocity between the injection position and extraction positions 2 and 3, the hydraulic communication between the injection position and extraction position 4, forming a competitive flow path in comparison to those connecting positions 2, 3 and the injection position, is enhanced; thus, outflow temperatures appear to drop slightly at observation position 4 under more hidden fractures.

While the number of fractures is fixed at four, the temperatures responses at the observation positions are predicted, following the variation of the fracture length from 20 to 160 m (Figure 4b), and the rotation of the hidden fracture by $\pm 20^{\circ}$ around its center position (Figure 4c), respectively. Variations on the fracture orientation and length lead to two groups of outflow temperatures at the three observation positions (breakthrough curves in Figures 4b and 4c). Under short fracture lengths and those orientations where fracture three is disconnected from fracture 1 (the index number annotated in Figures 4b and 4c), low outflow temperatures (Group 1) occur at positions 2 and 3 and are attributed to high flow velocity which occurs concentratedly in the flow paths between injection and these two observation positions; under the disconnected situations, variations of fracture orientation and length do not affect outflow temperatures at the observation positions. Once the hidden fracture connects fractures 3 and 1, with the increase of the fracture length or the hidden fracture placed with a proper orientation, outflow temperatures at positions 2 and 3 jump to a high value (Group 2); under the connected situation, the variation of fracture orientations and lengths becomes more important to the outflow temperature at positions 3 and 2.

Furthermore, the influence of the fracture aperture on the outflow temperature is investigated. It is found that temperatures at observation 2 and 3 increase with the fracture aperture, because the large aperture corresponds to a large cross-sectional area in fractures, and thus the flow velocity is reduced under constant injection and extraction rates; this enhances the matrix-fracture heat exchange along the flow path between the injection position and observation positions 2 and 3. A reverse trend occurs for the temperature at position 4.

The relative importance of one fracture parameter to the outflow temperature at a specific observation position is quantified as the ratio of the 30th-day-temperature variance provoked by the variation of one specific target parameter to the total variance of 30th-day temperatures induced by the variation of all fracture parameters. As summarized in Figure 4e, the temperatures at the three observation positions respond differently to a variation of the fracture parameters. At the observation position 2, outflow temperatures are mainly controlled by the fracture number, followed by the fracture aperture. At the observation position 3, temperatures are mainly controlled by the number and orientation of the hidden fracture. At the observation position 4, temperatures are primarily affected by the aperture.

Sensitivity analysis above indicates that (a) fracture parameters, especially fracture number, aperture, and orientation are sensitive to the outflow temperature, which can be inferred by fitting the calculated and observed temperatures, (b) temperatures monitored at more observation positions can better define fracture parameters, since the temperatures at different positions could shed light on specific fracture parameter(s), (c) multiple fracture parameters may affect the outflow temperature in the same manner (comparing effects of fracture number and aperture, and effects of fracture orientation and length); this would increase the uncertainty in fracture network characterization, which require additional constraints typically from geophysical data (i.e., MS data in this study).

4.1.2. Model Reliability

With temperature observations and MS events illustrated in Figure 2 as the input, the rjMCMC algorithm is implemented to estimate the fracture geometry and aperture. In this simple case, a single chain inversion model is employed. As shown in Figure 5, an initial fracture network composed by three fractures is generated, with the aperture of each fracture overestimated at 0.0065 m. After five iterations, the number of fractures is improved

JIANG ET AL.

19447973, 2023, 9, Downloaded

from https://agupubs.onlinelibrary.wiley.com/doi/10.1029/2022WR034339 by Eth Zirich Eth-Bibliothek, Wiley Online Library on [07.09/2023]. See the Terms and Conditions (https://onlinelibrary.wiley.com/terms-and-conditions) on Wiley Online Library for rules of use; OA articles are governous the conditions of the condit

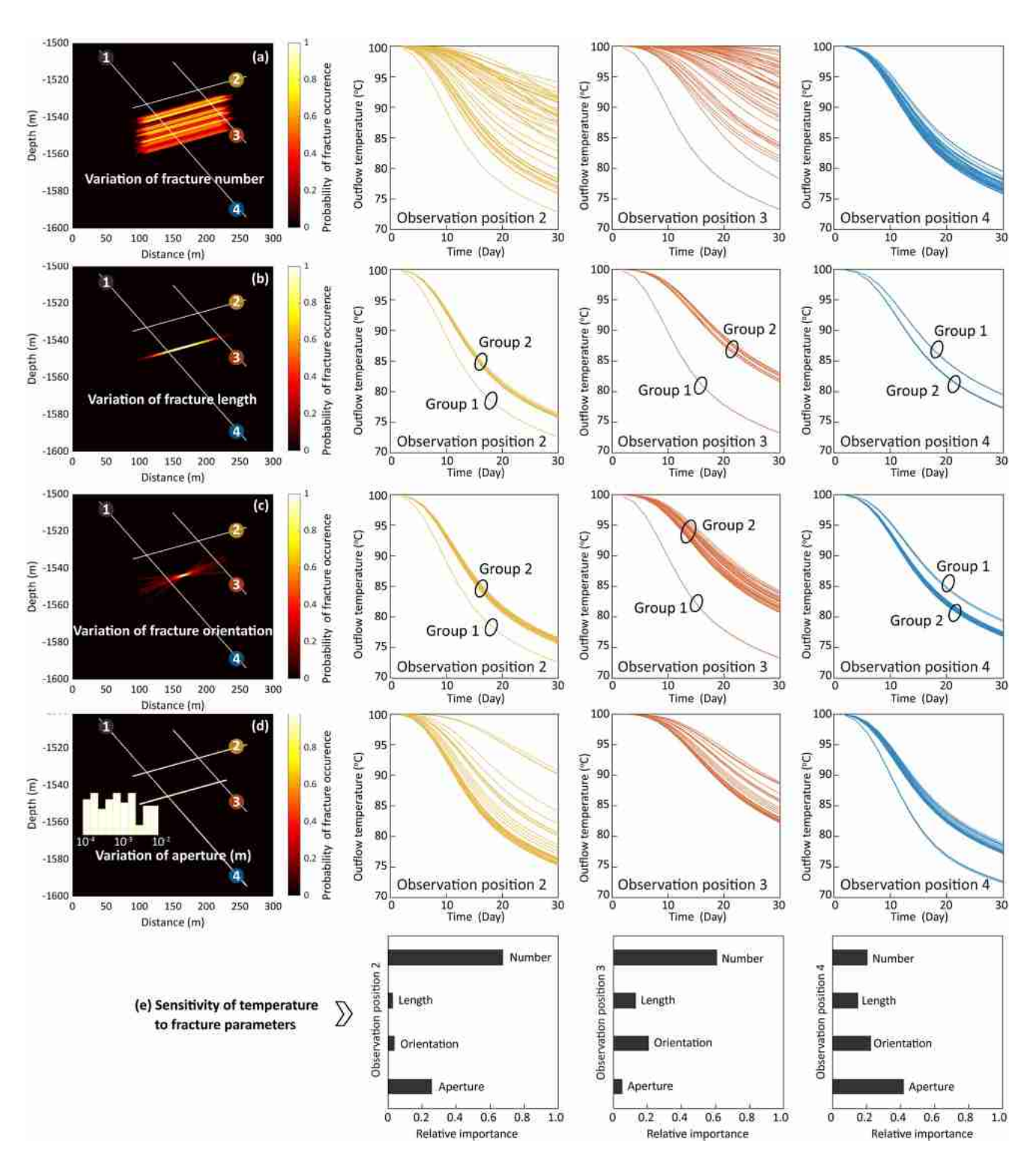


Figure 4. Outflow temperatures at observation position 2, 3, and 4 in response to (a) number, (b) length, (c) orientation, (d) aperture of the hidden fracture; and (e) relative importance of each fracture parameter to the temperatures at three observation positions.

to be four and the aperture is estimated at 0.0002 m. The model achieves a rapid convergence after 50 iterations, where the number of fractures stabilizes at four and the aperture is further improved and estimated at 0.0007 m. The misfit between calculated and observed temperatures stabilizes at approximately 1.0°C (equal to the measurement error). Considering the first 50 iterations as the burn-in period, the fracture realizations at 51 to 1,000

JIANG ET AL. 13 of 22

19447973, 2023, 9, Downle

ibrary on [07/09/2023].

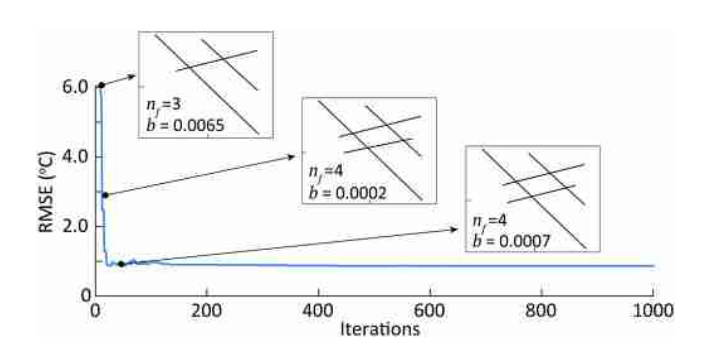


Figure 5. Trace plot of the misfit between calculated and observed temperatures, and fracture network realizations by 1, 5, and 50 iterations, respectively.

iterations along the single chain are stored, resulting in a probability map of the DFN (Figure 6b), as well as the misfit in breakthrough curves (Figure 6a).

As a result, the three fractures intersected by boreholes are accurately reconstructed (Figure 6b), with errors in fracture lengths and center positions that are well below 5% relative to the truth. The hidden fracture that is not intersected by the boreholes is also identified reliably. As illustrated in Table 1, the center location of this fracture drifts from the true fracture by less than 3.0 m (quantified by the distance in the vertical direction), with a mean error of 2.1 m. The discrepancy in the half-length between generated and true fracture is well controlled below 1.0 m with the mean of 0.5 m. With respect to the orientation, it is deviated by less than 5.0° featuring the mean value of 3.1°. Recalling that errors in the localization of MS events are assumed to range within ± 10 m and the variation in the prior orientations are given to be $\pm 10^\circ$, the inference of fracture network conditioned to both MS events and thermal breakthrough curves can significantly reduce errors in center locations, lengths and orientations of fractures.

The aperture of fractures is estimated in the range of 0.24–0.68 mm, which is in the same order of magnitude as the given true value of 1.0 mm. Still, the aperture is slightly underestimated. This is because in this synthetic case, outflow temperatures are less sensitive to the fracture aperture than to the fracture geometric pattern. Once the number, orientations, lengths and positions of fractures align with the truth, the thermal breakthrough curves

appear to fit well with observations, in response to the aperture varying from 0.24 to 0.68 mm.

4.1.3. Model Robustness

Due to the limitations in MS monitoring and interpretation techniques, errors always exist in the location of MS events in realistic field. In order to test its versatility, the performance of the inversion model is investigated under variant errors implemented in the location of MS events, following the uniform probability distribution within the range from (-5 m, 5 m) to (-40 m, 40 m), respectively. Each inversion model is run to convergence, with the RMSE of calculated and observed temperatures below 1.0°C (Equation 24). As illustrated in Figure 7, if the MS location error can be controlled below 5.0 m, the number of fractures is correctly identified as four, and the geometry of the hidden fracture can be mapped at high accuracy. The center position in the vertical direction differs from the truth by less than 0.5 m, the half-length by less than 2.0 m, and the orientation by less than 2.0°; the aperture is estimated at 0.36–0.96 mm, which approaches the true value of 1.0 mm. With the increase of MS location errors, both the mean error and the variation range of fracture parameters are generally enlarged. However, as long as errors in MS locations are kept below 20 m, which is equal to the distance (annotated as $D_{\rm m}$) between the hidden fracture and its nearest parallel fracture (i.e., fracture index marked as two in Figure 2a), the number of fractures can be accurately identified. The maximum difference in the center position of the hidden fracture is estimated at 5.0 m, in the half-length it is 17.0 m, and the maximum orientation difference is 5.0°, which are lower than the noise in MS locations and prior range of orientations, respectively. When further increasing the noise in MS locations to 30 m, equal to 1.5 $D_{\rm m}$, the number of fractures can still be determined as four, and errors in the fracture position and length can be well constrained. Although the error in fracture orientation increases to a maximum value of 8°, it is lower than the prior range of fracture orientation

When increasing errors in MS locations to 40 m, we reach values that are significantly higher than $D_{\rm m}$. In this case, the number of fractures fluctuates

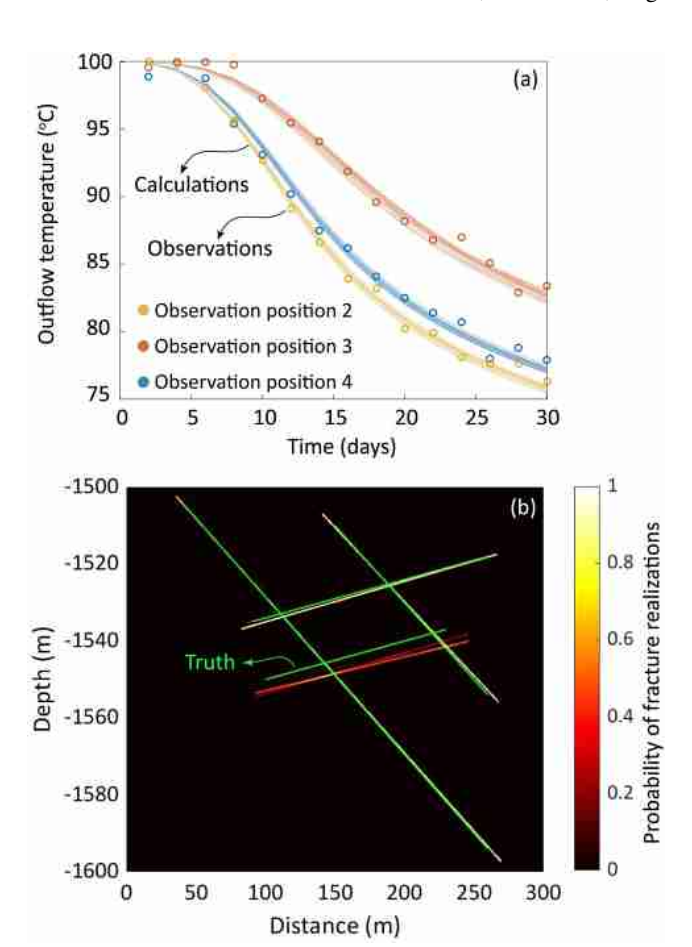


Figure 6. (a) Outflow temperatures in responses to (b) fracture realizations (expressed as the probability image defined by the frequency at each pixel after rasterizing the maps) generated by joint microseismic and temperature data inversion; both aligning with the truth.

JIANG ET AL. 14 of 22

 Table 1

 Errors in Estimating the Number of Fractures, and the Center Position, Half-Length, Orientation, and Aperture of the Hidden Fracture

Item	Fracture number	Center position (m)	Half-length (m)	Orientation	Aperture (m)
Truth	4	-1,546.5	65.3	84.3°	0.001
Realization1	4	-1,544.3	64.5	86°	0.0004
Realization2	4	-1,544.8	65.8	83°	0.0005
Realization3	4	-1,543.6	66.2	81°	0.0007
Mean value	4	-1,544.4	65.8	81.2°	0.0005
Mean error	0	2.1	0.5	3.1°	0.3ª

^aEstimated by the mean value of absolute errors after the logarithm conversion: llog10(Truth)-log10(Calculation)l, which indicate the magnitude of discrepancy.

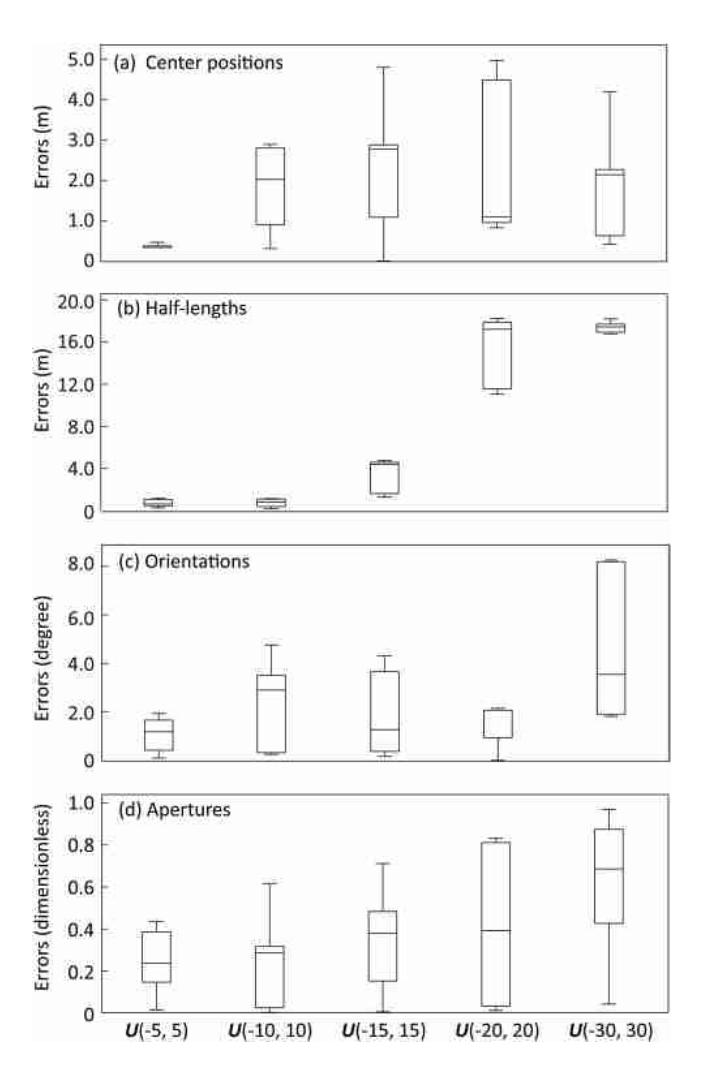


Figure 7. Estimation errors in (a) center position, (b) half-length, (c) orientation and (b) aperture of the hidden fracture under errors in microseismic locations assuming a uniform probability distribution of U(-5 m, 5 m), U(-10 m, 10 m), U(-15 m, 15 m), U(-20 m, 20 m), and U(-30 m, 30 m), respectively.

at three and four, and with respect to the mean aperture it generally varies reversely with the number of fractures. MS locations with high errors play only a minor role in constraining the uncertainty of fracture number and geometry. Adjacent fractures are possibly combined as one fracture featuring a larger aperture, which still results in sufficient accuracy in predicting the outflow temperatures. This indicates a limitation of the proposed method in predicting fracture network patterns in the highly fractured reservoir, which is defined by a low separation $(D_{\rm m})$ of two adjacent fractures relative to the noise $(E_{\rm m})$ in the interpreted MS locations in this study. In fractured reservoirs with $D_{\rm m}$ widely below $E_{\rm m}/1.5$, the method may fail to identify each fracture; rather, the adjacent fractures tend to be merged as one fracture. In that case, a heterogeneous continuum conceptual model of the reservoir, that is, a spatial distribution of permeability, might be favorable (Dong et al., 2019).

Despite the high uncertainty in the prior estimations of fracture geometry attributed to the high errors in MS locations, the evaluation of the generated DFN realization based on the MS events in the likelihood function yields posterior realizations that fulfill the measured temperature data with the RMSE converged to below 1°C. A smaller error in the location of the MS events improves the prior DFN generation. It reduces the number of possible posterior DFN realizations leading to a better resolution in the fracture probability map.

Analyses above indicate that the joint inversion of MS data and thermal breakthrough data can reduce the error and uncertainty in fracture length, position, and orientation, which are well below those informed by merely MS data and prior estimations; the model can also estimate the fracture aperture in the same magnitude as the true value. However, errors and uncertainties in fracture parameters tend to increase with the error in MS locations. The interpretation of MS locations to higher accuracy is desirable for high-quality fracture network characterization by using the proposed inversion framework; the error of MS locations below 1.5 D_m is considered as a precondition to correctly separate the fractures with the distance of D_m .

Furthermore, the performance of the inversion model is examined under other reservoir conditions and varying types of observation data. With the reservoir conditions and observation data provided in Section 3.1 as the base case, (a) the thermal conductivity of rock matrix is increased to 8.0 W·(m·°C)⁻¹ in comparison to 2.0 W·(m·°C)⁻¹, to clarify the performance of the inversion model under variant fracture-matrix heat exchange rates; (b) the density

JIANG ET AL. 15 of 22

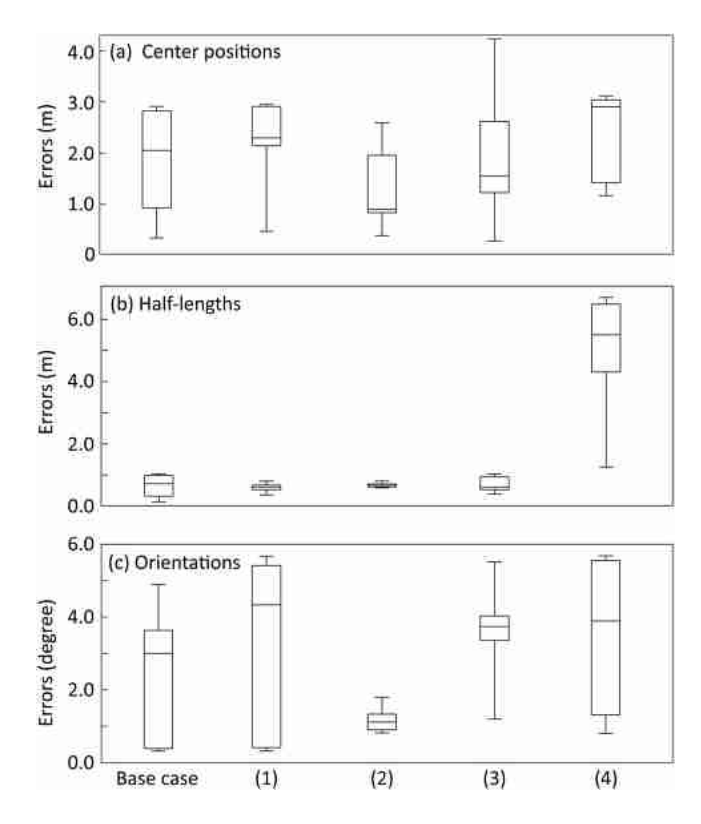


Figure 8. Estimation errors in (a) center positions, (b) half-lengths, and (c) orientations of the hidden fracture under the base case, in comparison with (1) thermal conductivity of rock matrix increasing to 8.0 W·(m·°C)⁻¹, (2) consideration of density-dependent flow and under initial thermal gradient 6°C/100 m, (3) use of pressure as additional constraint for fracture inversion, and (4) unknown fracture orientations at the positions of fracture intersecting boreholes.

and viscosity variation with temperature is considered under uneven initial temperature distribution following a geothermal gradient of 6.0°C/100 m, in order to test the potential influence of density-driven flow on the fracture network characterization. (c) pressures at observation positions are employed as additional data for the inference of fracture geometry, and (d) fracture orientations at the positions of fractures intersecting boreholes are assumed to be unknown, in order to test if the model performance can be significantly affected by the types of data possibly available in deep reservoirs.

There is no trending variation in estimated apertures and fracture numbers, but the statistics of fracture positions, lengths and orientations vary partly under the conditions above. Firstly, the thermal conductivity is increased from 2.0 to 8.0 W·(m·°C) $^{-1}$, which represents an uncommonly high thermal conductivity but to emphasize the influence of fracture-matrix heat exchange; consequently, the center position, length, and orientation of the hidden fracture to fluctuate in the similar range featuring close mean values (Figure 8). This suggests that the performance of the model is unaffected by the magnitude of thermal conductivity and fracture-matrix heat exchange, as long as the forward model of flow and heat transport can describe the process of fracture-matrix heat exchange accurately.

The consideration of density-driven flow (i.e., density and viscosity variation with temperature) in the forward model can reduce the error and uncertainty in predicting the position, especially the orientation, of the hidden fracture (Figure 8c); this is because outflow temperatures in response to the density-driven flow are related to the dip angle of fractures. On the one hand, this represents an advantage of using temperature as tracer, which can improve the accuracy of fracture network characterization in geothermal reservoirs; on the other hand, the consideration of density-driven flow in the forward model increases the computational burden significantly. In these illustrated cases, single computation of the forward model without considering density effects takes 30−40 s on the desktop computer (Intel Core™ i9-9900 CPU 3.6 GHz), but takes 300−500 s once the density effects are considered. In the low-to-median enthalpy geothermal reservoirs filled with liquid water, the

fluid density variation with hydraulic pressure is often neglected, since the average density change versus pressure is estimated at about $0.4~\rm kg/m^3$ per Mega Pascal (MPa), in comparison to an average density change versus temperature of about $0.5~\rm kg/m^3$ per Degree Celsius (°C) (Cooper & Dooley, 2007; Wagner & Pruß, 2002). In the illustrated examples, the density variation induced by the hydraulic pressure is lower than $1.0~\rm kg/m^3$ (in response to the maximum pressure difference in the reservoir below $2.0~\rm MPa$), which is significantly lower than the density variation induced by the temperature of $15~\rm kg/m^3$ (in response to the maximum temperature difference of $30~\rm C$). Similarly, the effect of pressure on the water viscosity is also negligible in comparison to that of temperature (Cooper & Dooley, 2007; Wagner & Pruß, 2002).

Under the given hydraulic and thermal conditions in the illustrated case, pressures at three observation positions reach steady state immediately. Thus, the inclusion of pressure observations as additional data besides to temperatures and MS locations does not improve the accuracy in characterizing the fracture geometry (Figures 8a–8c). Lastly, the influence of borehole information on the fracture characterization is investigated. In the base case, orientation of fractures at positions of fractures intersecting boreholes are assumed to be deterministic. For comparison, the fracture orientation at the borehole wall is now assumed to be unknown. The corresponding inversion results reveal that pre-defined fracture orientation at borehole walls, orientations and positions of the hidden fracture can be estimated to the accuracy at the same level to the model with deterministic fracture orientation at borehole walls. However, larger errors and uncertainties exist in estimating the lengths of the hidden fractures (Figure 8b). This is because without pre-defined orientations to the fractures on the borehole wall, there is a higher possibility that MS events belonging to the neighboring fracture are wrongly categorized to the hidden fracture; thus, the fracture size determined by the projection of MS events on the fracture plane could be deviated from the truth.

JIANG ET AL. 16 of 22

19447973, 2023, 9, Downloaded

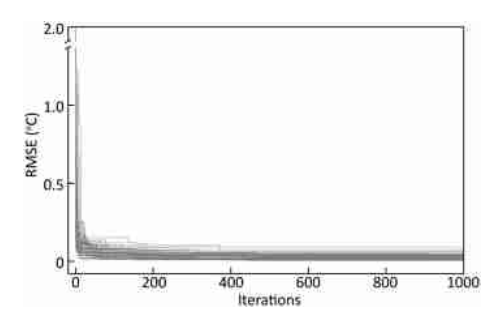


Figure 9. Trace plot of the misfit between observed and calculated outflow temperatures.

4.2. Outcrop-Based Case

4.2.1. Model Reliability

To further examine the effectiveness of the inversion model in recreating the complex fracture network, the outcrop-based fracture network is inferred by rjMCMC inversion, along 100 independent chains by parallel computing. As shown in Figure 9, the misfits between calculated and observed temperatures decrease rapidly along each chain, with the value stabilizing below 0.1 after 400 iterations. It was tested that further increasing the number of iterations to 2,000, the misfit in temperature does not reduce, and the acceptance ratio of the inversion model approaches zero. Thus, the inversion model reaches convergence, and the first 400 iterations are regarded as the burn-in period.

Realizations of fracture networks at the 1,000th iteration of 100 chains are extracted, that is, one realization is extracted from each chain and a total of

100 realizations are stored. As shown in Table 2, the error in the number of fractures is estimated at 1 to 3, and the mean error in fracture lengths and orientations is estimated at 1.5° and 5.0 m, respectively. The aperture of fractures is estimated at 0.70–6.3 mm, with a mean value of 3.6 mm. The aperture is well constrained to the same order of magnitude as the true value of 1.0 mm, although it is slightly overestimated. This is because the proposed method tends to combine the fractures featuring similar orientations and a separation lower than the error range of MS events as one fracture (see Section 4.1). Thus, the number of identified fractures in this synthetic case is underestimated at 14 to 16, which is less than the true value of 17. The reduced number of fractures is compensated by an increase in the fracture aperture.

The realizations of fracture network results in a probability map of fracture network (Figures 10b–1) and a misfit between calculated and observed breakthrough curves (Figures 10a–1). A direct comparison between true fractures and the probability map shows that the fractures revealed by downhole logs with predefined orientations can be accurately recreated, with errors in length and center position below 10% relative to the truth. Other fractures that are not revealed by the downhole logs fit well with a fracture probability higher than 50% (Figures 10b–1). This suggests that the proposed method is capable of reconstructing major features of the fracture network, while predicting the thermal breakthrough curves well.

The reliability of the joint inversion procedure for reconstructing fracture network is further examined by predicting the thermal breakthrough curve in the alternative trial production test (Section 3.3). As shown in Figures 10c–1, the thermal breakthrough curves in response to 100 realizations of fracture network in Figures 10b–1 align with the observations of the validation dataset. The mean error in temperature prediction is less than 1.0°C (equilibrium to approximately 4% of the temperature variation in 30-day production), representing a particularly

good performance of the inverted models for the prediction of heat transport and heat production.

Table 2 *Errors in Estimating the Number, Orientations, Lengths, and Apertures of Fractures*

	Fracture	Orientations		Lengths	Apertures
Item	number	Group 1	Group 2	(m)	(m)
Truth	17	22–35°	114–122°	17–111	0.001
Statistics	17	29.5°	119.5°	54.4	0.001
Realization1	14	29-35°	120–123°	19–117	0.006
Realization2	16	21–34°	116–122°	19–118	0.002
Realization3	15	23-30°	120–124°	12-118	0.0007
Statistics	14–16	28.0°	120.1°	59.4	0.004
Mean error	1–3	1.5°	0.6°	5.0	0.6ª

^aError after logarithm conversion, indicating the error expressed by the magnitude.

4.2.2. Model Comparison

For highlighting the complementarity of MS and temperature data for inversion of the outcrop-based case, the joint MS and temperature data inversion is additionally compared to a pure temperature data inversion without using seismicity information. The latter represents a traditional inversion model for fracture tomography (Ringel et al., 2019; Somogyvári et al., 2017). Both inversion models are iterated 1,000 times over 100 chains. It is revealed that when including MS events, the misfits in outflow temperatures decrease rapidly during the first 50 iterations, and over 90% of chains they stabilize at the value below 0.1°C after 200 iterations. Accordingly, the burn-in period is estimated to range over 400 iterations (Figure 9). In contrast, without MS data, the misfits in temperatures at merely 20% of chains drop to 0.1°C after 400 iterations, and at less than 40% of chains they stabilize after 1,000 iterations at values below 0.1°C, while the others struggle to achieve the convergence even after 2,000 iterations. Including MS events can significantly

JIANG ET AL. 17 of 22

19447973, 2023, 9, Downloaded from https://gupubs.onlinelibrary.wiley.com/doi/10.1029/2022WR034339 by Eth Zürich Eth-Bibliothek, Wiley Online Library on [07.09/2023]. See the Terms

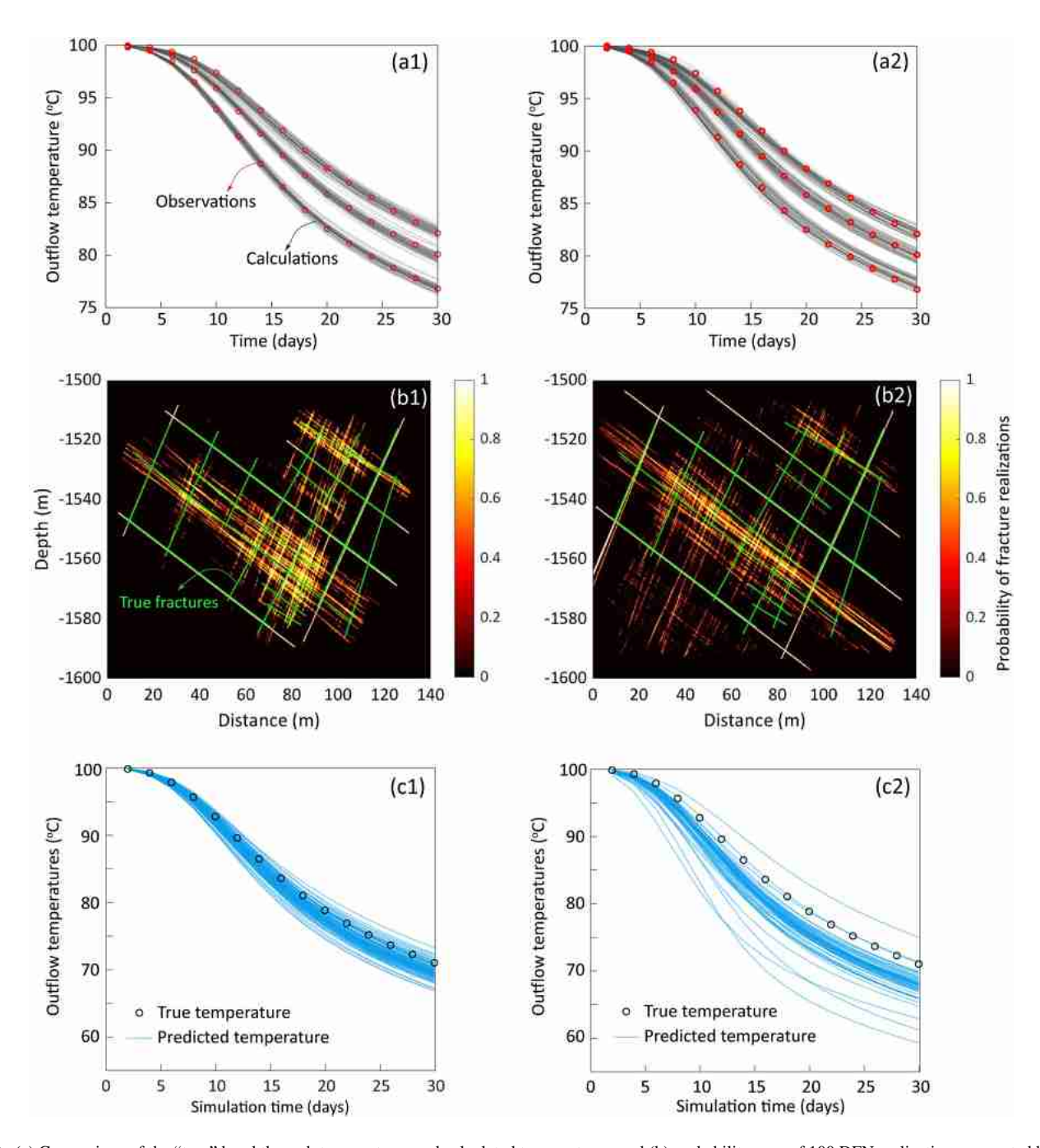


Figure 10. (a) Comparison of the "true" breakthrough temperatures and calculated temperatures, and (b) probability map of 100 DFN realizations generated by (a) joint inversion and (b) pure temperature data inversion, and (c) thermal breakthrough curve associated with each DFN realization compared to the observed temperature in the validation step.

shorten the burn-in period and save computation time by providing geometric information for the efficient generation of DFN realizations.

Moreover, the generation of DFN realizations from MS events reduces the uncertainty of the inversion results (Figure 10b) and it enables a more accurate prediction of the temperature profiles (Figure 10c). The effect of integrating the MS events facilitates a better resolution of the fracture probability map in the lower left of the investigated region. Without the application of the MS events, several fractures with a probability of approximately 50% appear in Figure 10b–2 in contrast to Figure 10b–1. Also, the lengths of fractures are generally overestimated when not considering the information from MS events.

JIANG ET AL. 18 of 22

With the priors on the orientations defined by downhole logs, the orientations of fractures intersected by boreholes can be well identified by both the pure temperature data inversion and by the joint inversion. However, higher uncertainties in the fracture parameters lead to higher errors in predicting outflow temperatures. This is observed for both inversion and validation periods for the traditional inversion, where the misfit between calculated and observed temperature reaches 3° C, which is larger than the mean observation errors of 0.1° C (Figure 10a-2). Based on the generated fracture networks, the outflow temperature predicted in the validation dataset deviates from the observations by -5° C to 15° C, with a mean error over 5° C (Figure 10c-2). In contrast, the uncertainty is significantly reduced by joint inversion (Figure 10c-1).

4.3. Outlooks

Joint MS and thermal breakthrough data inversion enables the inference of fracture number orientation and aperture. It improves estimation of fracture size and position with errors significantly lower than errors in the locations of MS events. However, errors in fracture parameters tend to increase with the errors in the locations of MS events. The presented analyses with synthetic examples demonstrated that the inversion model tends to combine adjacent fractures as single one with larger aperture, if the error in MS events (annotated as E_w) increases beyond $1.5 D_m$ (i.e., the minimum distance between two adjacent fractures). As revealed by the outcrop-based cases, the number of fractures is estimated to be lower than the true value of 17 and the aperture is estimated higher than 1.0 mm. This results in the average outflow temperature lower than the observations by about 1.0°C for 30-day production (Figure 10c). Although this is merely equal to approximately 4% of the temperature variation, representing a sufficiently accurate estimation, there is still a risk that this error becomes even higher in realistic implementation where high errors in the MS locations or low fracture separations in highly fractured reservoir occur. Based on the findings with the synthetic case, the resolution of the inversion model in identifying adjacent fracture is approximately $E_m/1.5$. For example, when the noise in the location of MS events is 15 m, the minimum distance between two adjacent fractures to be well separated is 10 m. A distance lower than 10 m tends to yield a single fracture with larger aperture. Moreover, part of tiny fractures may lead to extremely weak seismic signals, which cannot be captured by the seismic stations and reflected by the MS events. In order to address these problems, high-quality localization of MS events is preferred, in order to improve the accuracy in the interpretation of fracture networks. An alternative way is to simulate the physical processes of MS generation during hydraulic fracturing adhering to the forward flow and tracer transport modeling under the rjMCMC inversion framework; this will increase the computational burden, but is an objective for future research.

Although we focused on a 2D problem, the framework of the inversion model in generating a fracture network from MS events and tracer data is transferable to the 3D implementation. For this, the input parameter of orientation (s) needs to be replaced by dip angle and strike, and the fracture length (l) needs to be replaced by length and width assuming the shape of fracture features, for example, a plane rectangle. The rjMCMC approach for fracture network updating is also applicable to the characterization of 3D fracture parameters (Equations 10 and 11) (Ringel et al., 2022). The effect of the inversion framework was demonstrated by applying heat as tracer. Heat is often employed to mimic the chemical-reactive tracer in the interpretation or validation of reservoir structure (Ren et al., 2023; Saar, 2011; Wu et al., 2021), attributed to its cost-effectiveness without adding chemical species into the reservoir. It is best suit for geothermal reservoirs, since heat as a tracer is closer to geothermal applications than chemical tracers. For example, strong heat dissipation observed through tracer test also indicates a strong heat dissipation when operating a geothermal plant. However, the heat dissipation would lead to weak temperature responses in realistic 3D fractured reservoirs. Thus, for implementations in practice, thermal tracer often works with other conservative and reactive tracers. Multiple-tracer interpretation can be incorporated into the proposed inversion framework by replacing the governing equations for heat transport (Equation 6) with the equations for advection-dispersion, for the simulation of tracer transport and the misfit between calculated and observed concentration (Equation 9).

In general, the implementation of the inversion model for realistic and 3D fracture network characterization is potentially limited by the computational efficiency of the forward flow and transport model in complex 3D fracture networks. Replacing the 2D simulator THERMAID by a high-performance 3D DFN simulator, for example, DFNWORKs, and using a conservative tracer instead of temperature, would allow forward modeling of flow and transport in the fracture network efficiently by neglecting the fracture-matrix tracer exchange and tracer transport in the matrix. The integrated inversion model for 3D fracture network characterization will be tested in the future

JIANG ET AL. 19 of 22

19447973, 2023, 9, Downloaded

for the conditions at enhanced geothermal systems of the Gonghe site, China, where MS events have been monitored during the reservoir stimulation and two-stage tracer tests have been conducted.

5. Conclusions

This study established a novel inversion framework to characterize the DFN by integrating seismicity and temperature data with the rjMCMC algorithm. The inversion model was tested in two synthetic fractured geothermal reservoirs composed of four fractures and fracture reservoir featuring 17 fractures, respectively. The model enabled the estimation of the fracture number, orientations, positions, lengths and aperture reliably. Based on the realizations of fracture networks, the heat production can be accurately predicted with a mean error lower than 5%.

Regarding the data availability in realistic deep reservoirs, the proposed inversion model merely required the minimum number of fractures and gross fracture orientation ranges revealed by downhole logs, thermal breakthrough curves obtained in the trial-production test via doublet wells, and MS events monitored during reservoir stimulation. It was best suited for the fracture network characterization in enhanced geothermal reservoirs and unconventional gas/oil reservoirs, where the MS events are monitored, and trial-production test data are available. Fracture networks can be generated reliably. In contrast, supported by the same amount of temperature data without seismicity information, the traditional inversion model overestimated the fracture size, and led to severely biased prediction on heat production with high uncertainty.

Overall, the application of MS events and thermal breakthrough curves for the joint DFN inversion complemented each other. Recorded MS events provided information about the structural properties of the fractured rock to be applied for the efficient generation of DFN realizations and the temperature curves are the basis to also adjust the hydraulic properties of the DFN. The proposed algorithm formed a cost-efficient way to image the DFN without requirement of the massive hydraulic and tracer data observations by cross-well multiple-source-and-receiver test.

Data Availability Statement

The data files for this research, including the microseismicity data and temperature data employed to test the inversion model, are available via the Harvard Dataverse (Jiang, 2022b).

Software Availability Statement: Software for this research includes the codes for the forward modeling and the inversion. The forward modeling employed the open source codes THERMAID, which can be requested via (Jansen et al., 2018). The source codes developed in this research for joint microseismicity and tracer test data inversion are available via the Harvard Dataverse (Jiang, 2022a).

References

AbuAisha, M., Loret, B., & Eaton, D. (2016). Enhanced geothermal systems (EGS): Hydraulic fracturing in a thermo-poroelastic framework. Journal of Petroleum Science and Engineering, 146, 1179–1191. https://doi.org/10.1016/j.petrol.2016.07.027

Afshari Moein, M. J., Somogyvári, M., Valley, B., Jalali, M., Loew, S., & Bayer, P. (2018). Fracture network characterization using stress-based tomography. *Journal of Geophysical Research: Solid Earth*, 123(11), 9324–9340. https://doi.org/10.1029/2018jb016438

Aminzadeh, F., Tafti, T. A., & Maity, D. (2013). An integrated methodology for sub-surface fracture characterization using microseismic data: A case study at the NW Geysers. *Computers & Geosciences*, 54, 39–49. https://doi.org/10.1016/j.cageo.2012.10.015

Berkowitz, B. (2002). Characterizing flow and transport in fractured geological media: A review. Advances in Water Resources, 25(8-12), 861-884. https://doi.org/10.1016/s0309-1708(02)00042-8

Bodin, T., & Sambridge, M. (2009). Seismic tomography with the reversible jump algorithm. *Geophysical Journal International*, 178(3), 1411–1436. https://doi.org/10.1111/j.1365-246x.2009.04226.x

Brauchler, R., Böhm, G., Leven, C., Dietrich, P., & Sauter, M. (2013). A laboratory study of tracer tomography. *Hydrogeology Journal*, 21(6), 1265–1274. https://doi.org/10.1007/s10040-013-1006-z

Brudy, M., & Zoback, M. (1999). Drilling-induced tensile wall-fractures: Implications for determination of in-situ stress orientation and magnitude. *International Journal of Rock Mechanics and Mining Sciences*, 36(2), 191–215. https://doi.org/10.1016/s0148-9062(98)00182-x

Bruel, D. (2002). Impact of induced thermal stresses during circulation tests in an engineered fractured geothermal reservoir: Example of the Soultz-sous-Forets European hot fractured rock geothermal project, Rhine Graben, France. *Oil and Gas Science and Technology*, 57(5), 459–470. https://doi.org/10.2516/ogst:2002030

Cooper, J., & Dooley, R. (2007). Revised release on the IAPWS industrial formulation 1997 for the thermodynamic properties of water and steam. The International Association for the Properties of Water and Steam, 1, 48.

Cornet, F. H. (2000). Comment on 'Large-scale in situ permeability tensor of rocks from induced microseismicity' by SA Shapiro, P. Audigane and J.-J. Royer. *Geophysical Journal International*, 140(2), 465–469. https://doi.org/10.1046/j.1365-246x.2000.00018.x

Acknowledgments

Funding support for this study was provided by the National Key R&D Program of China (2018YFB1501803) and the National Natural Science Foundation of China (42172268). Additional funding was provided by Carbon Peak and Carbon Neutralization Science and Technology Innovation Special Fund of Jiangsu Province, China (BE2022859). The contributions by L.M.R. and P.B. to this study were funded by the German Research Foundation (DFG), Grant BA-2850-5-1. We thank Siyuan Li for generating the synthetic microseismic data for model verification, and Ryan Pearson for proofreading.

JIANG ET AL. 20 of 22

- Cornet, F. H., Bérard, T., & Bourouis, S. (2007). How close to failure is a granite rock mass at a 5 km depth? *International Journal of Rock Mechanics and Mining Sciences*, 44(1), 47–66. https://doi.org/10.1016/j.ijrmms.2006.04.008
- Darcel, C., Bour, O., & Davy, P. (2003). Stereological analysis of fractal fracture networks. Journal of Geophysical Research, 108(B9). https://doi.org/10.1029/2002jb002091
- Day-Lewis, F. D., Hsieh, P. A., & Gorelick, S. M. (2000). Identifying fracture-zone geometry using simulated annealing and hydraulic-connection data. Water Resources Research, 36(7), 1707–1721. https://doi.org/10.1029/2000wr900073
- De Dreuzy, J. R., Méheust, Y., & Pichot, G. (2012). Influence of fracture scale heterogeneity on the flow properties of three-dimensional discrete fracture networks (DFN). *Journal of Geophysical Research*, 117(B11). https://doi.org/10.1029/2012jb009461
- Dong, Y., Fu, Y., Yeh, T. C. J., Wang, Y. L., Zha, Y., Wang, L., & Hao, Y. (2019). Equivalence of discrete fracture network and porous media models by hydraulic tomography. Water Resources Research, 55(4), 3234–3247. https://doi.org/10.1029/2018wr024290
- Dorn, C., Linde, N., Borgne, T. L., Bour, O., & De Dreuzy, J.-R. (2013). Conditioning of stochastic 3-D fracture networks to hydrological and geophysical data. *Advances in Water Resources*, 62, 79–89. https://doi.org/10.1016/j.advwatres.2013.10.005
- Fadakar Alghalandis, Y., Dowd, P. A., & Xu, C. (2013). The RANSAC method for generating fracture networks from micro-seismic event data. Mathematical Geosciences, 45(2), 207–224. https://doi.org/10.1007/s11004-012-9439-9
- Farooq, M., Nisar, U. B., Khan, S., Jalees, T., Mughal, M. R., Ali, L., & Ahmed, T. (2022). Electrical resistivity tomography for delineating groundwater potential zones in fractured metasedimentary rocks, Lesser Himalayas, Pakistan. *Journal of Earth System Science*, 131(2), 1–14. https://doi.org/10.1007/s12040-022-01863-8
- Folesky, J., Kummerow, J., Shapiro, S. A., Häring, M., & Asanuma, H. (2016). Rupture directivity of fluid-induced microseismic events: Observations from an enhanced geothermal system. *Journal of Geophysical Research: Solid Earth*, 121(11), 8034–8047. https://doi.org/10.1002/2016jb013078
- Green, P. J. (1995). Reversible jump Markov chain Monte Carlo computation and Bayesian model determination. *Biometrika*, 82(4), 711–732. https://doi.org/10.1093/biomet/82.4.711
- Hajibeygi, H., Karvounis, D., & Jenny, P. (2011). A hierarchical fracture model for the iterative multiscale finite volume method. *Journal of Computational Physics*, 230(24), 8729–8743. https://doi.org/10.1016/j.jcp.2011.08.021
- Hyman, J., Dentz, M., Hagberg, A., & Kang, P. K. (2019). Linking structural and transport properties in three-dimensional fracture networks. Journal of Geophysical Research: Solid Earth, 124(2), 1185–1204. https://doi.org/10.1029/2018jb016553
- Illman, W. A., Liu, X., Takeuchi, S., Yeh, T. C. J., Ando, K., & Saegusa, H. (2009). Hydraulic tomography in fractured granite: Mizunami underground research site, Japan. Water Resources Research, 45(1). https://doi.org/10.1029/2007wr006715
- Jansen, G., Valley, B., & Miller, S. A. (2018). THERMAID-A matlab package for thermo-hydraulic modeling and fracture stability analysis in fractured reservoirs. arXiv preprint arXiv:1806.10942.
- Jiang, Z. (2022a). Source codes for discrete fracture networks tomography by joint inversion of microseismicity and thermal breakthrough data (Software). Harvard Datayerse, https://doi.org/10.7910/DVN/TAP27P
- Jiang, Z. (2022b). Test data for discrete fracture networks tomography [dataset]. Harvard Dataverse. https://doi.org/10.7910/DVN/VY7120
- Jiang, Z., Zhang, S., Turnadge, C., & Xu, T. (2021). Combining autoencoder neural network and Bayesian inversion to estimate heterogeneous permeability distributions in enhanced geothermal reservoir: Model development and verification. Geothermics, 97, 102262. https://doi.org/10.1016/j.geothermics.2021.102262
- Klepikova, M., Brixel, B., & Jalali, M. (2020). Transient hydraulic tomography approach to characterize main flowpaths and their connectivity in fractured media. *Advances in Water Resources*, 136, 103500. https://doi.org/10.1016/j.advwatres.2019.103500
- Lehujeur, M., Vergne, J., Schmittbuhl, J., Zigone, D., Le Chenadec, A., & Team, E. (2018). Reservoir imaging using ambient noise correlation from a dense seismic network. *Journal of Geophysical Research: Solid Earth*, 123(8), 6671–6686. https://doi.org/10.1029/2018jb015440
- Liu, Q., Hu, R., Hu, L., Xing, Y., Qiu, P., Yang, H., et al. (2022). Investigation of hydraulic properties in fractured aquifers using cross-well travel-time based thermal tracer tomography: Numerical and field experiments. *Journal of Hydrology*, 609, 127751. https://doi.org/10.1016/j.ihvdrol.2022.127751
- Long, J. C., Remer, J., Wilson, C., & Witherspoon, P. (1982). Porous media equivalents for networks of discontinuous fractures. Water Resources Research, 18(3), 645–658. https://doi.org/10.1029/wr018i003p00645
- Maillot, J., Davy, P., Le Goc, R., Darcel, C., & De Dreuzy, J. R. (2016). Connectivity, permeability, and channeling in randomly distributed and kinematically defined discrete fracture network models. Water Resources Research, 52(11), 8526–8545. https://doi.org/10.1002/2016wr018973
- Majer, E. L., Baria, R., Stark, M., Oates, S., Bommer, J., Smith, B., & Asanuma, H. (2007). Induced seismicity associated with enhanced geothermal systems. Geothermics, 36(3), 185–222. https://doi.org/10.1016/j.geothermics.2007.03.003
- Marrett, R., Ortega, O. J., & Kelsey, C. M. (1999). Extent of power-law scaling for natural fractures in rock. *Geology*, 27(9), 799–802. https://doi.org/10.1130/0091-7613(1999)027<0799:eoplsf>2.3.co;2
- Maxwell, S. C. (2014). Microseismic imaging of hydraulic fracturing: Improved engineering of unconventional shale reservoirs. Society of Exploration Geophysicists.
- Maxwell, S. C., Chorney, D., & Goodfellow, S. (2015). Microseismic geomechanics of hydraulic-fracture networks: Insights into mechanisms of microseismic sources. The Leading Edge, 34(8), 904–910. https://doi.org/10.1190/tle34080904.1
- Maxwell, S. C., Mack, M., Zhang, F., Chorney, D., Goodfellow, S., & Grob, M. (2015). Differentiating wet and dry microseismic events induced during hydraulic fracturing. Paper presented at unconventional resources technology conference, San Antonio, Texas, 20-22 July 2015. Society of Exploration Geophysicists, American Association of Petroleum.
- Maxwell, S. C., Shemeta, J., Campbell, E., & Quirk, D. (2008). Microseismic deformation rate monitoring, paper presented at SPE Annual Technical Conference and Exhibition. *OnePetro*.
- McKean, S., Priest, J., Dettmer, J., & Eaton, D. (2019). Quantifying fracture networks inferred from microseismic point clouds by a Gaussian mixture model with physical constraints. Geophysical Research Letters, 46(20), 11008–11017. https://doi.org/10.1029/2019gl083406
- Nejadi, S., Trivedi, J. J., & Leung, J. (2017). History matching and uncertainty quantification of discrete fracture network models in fractured reservoirs. *Journal of Petroleum Science and Engineering*, 152, 21–32. https://doi.org/10.1016/j.petrol.2017.01.048
- Neuman, S. P. (2005). Trends, prospects and challenges in quantifying flow and transport through fractured rocks. *Hydrogeology Journal*, 13(1), 124–147. https://doi.org/10.1007/s10040-004-0397-2
- Ren, Y., Kong, Y., Pang, Z., & Wang, J. (2023). A comprehensive review of tracer tests in enhanced geothermal systems. *Renewable and Sustainable Energy Reviews*, 182, 113393. https://doi.org/10.1016/j.rser.2023.113393
- Ringel, L. M., Jalali, M., & Bayer, P. (2021). Stochastic inversion of three-dimensional discrete fracture network structure with hydraulic tomography. Water Resources Research, 57(12), e2021WR030401. https://doi.org/10.1029/2021wr030401
- Ringel, L. M., Jalali, M., & Bayer, P. (2022). Characterization of the highly fractured zone at the Grimsel Test Site based on hydraulic tomography. Hydrology and Earth System Sciences, 26(24), 6443–6455. https://doi.org/10.5194/hess-26-6443-2022

JIANG ET AL. 21 of 22

- Ringel, L. M., Somogyvári, M., Jalali, M., & Bayer, P. (2019). Comparison of hydraulic and tracer tomography for discrete fracture network inversion. Geosciences, 9(6), 274. https://doi.org/10.3390/geosciences9060274
- Saar, M. O. (2011). Geothermal heat as a tracer of large-scale groundwater flow and as a means to determine permeability fields. *Hydrogeology Journal*, 19(1), 31–52. https://doi.org/10.1007/s10040-010-0657-2
- Schöniger, A., Nowak, W., & Hendricks Franssen, H. J. (2012). Parameter estimation by ensemble Kalman filters with transformed data: Approach and application to hydraulic tomography. Water Resources Research, 48(4). https://doi.org/10.1029/2011wr010462
- Schuite, J., Longuevergne, L., Bour, O., Guihéneuf, N., Becker, M. W., Cole, M., et al. (2017). Combining periodic hydraulic tests and surface tilt measurements to explore in situ fracture hydromechanics. *Journal of Geophysical Research: Solid Earth*, 122(8), 6046–6066. https://doi.org/10.1002/2017jb014045
- Shapiro, S. A., Audigane, P., & Royer, J.-J. (1999). Large-scale in situ permeability tensor of rocks from induced microseismicity. *Geophysical Journal International*, 137(1), 207–213. https://doi.org/10.1046/j.1365-246x.1999.00781.x
- Shapiro, S. A., Dinske, C., & Rothert, E. (2006). Hydraulic-fracturing controlled dynamics of microseismic clouds. *Geophysical Research Letters*, 33(14), L14312. https://doi.org/10.1029/2006gl026365
- Somogyvári, M., Jalali, M., Jimenez Parras, S., & Bayer, P. (2017). Synthetic fracture network characterization with transdimensional inversion. Water Resources Research, 53(6), 5104–5123. https://doi.org/10.1002/2016wr020293
- Tchalenko, J. (1970). Similarities between shear zones of different magnitudes. Geological Society of America Bulletin, 81(6), 1625–1640. https://doi.org/10.1130/0016-7606(1970)81[1625:sbszod]2.0.co;2
- Tiedeman, C. R., & Barrash, W. (2020). Hydraulic tomography: 3D hydraulic conductivity, fracture network, and connectivity in Mudstone. *Groundwater*, 58(2), 238–257. https://doi.org/10.1111/gwat.12915
- Valley, B. C. (2007). The relation between natural fracturing and stress heterogeneities in deep-seated crystalline rocks at Soultz-sous-Forêts (France). ETH Zurich.
- Vidal, J., Genter, A., & Chopin, F. (2017). Permeable fracture zones in the hard rocks of the geothermal reservoir at Rittershoffen, France. *Journal of Geophysical Research: Solid Earth*, 122(7), 4864–4887. https://doi.org/10.1002/2017jb014331
- Vu, M., & Jardani, A. (2022). Mapping discrete fracture networks using inversion of hydraulic tomography data with convolutional neural network: SegNet-fracture. *Journal of Hydrology*, 609, 127752. https://doi.org/10.1016/j.jhydrol.2022.127752
- Wagner, W., & Pruß, A. (2002). The IAPWS formulation 1995 for the thermodynamic properties of ordinary water substance for general and scientific use. *Journal of Physical and Chemical Reference Data*, 31(2), 387–535. https://doi.org/10.1063/1.1461829
- Wang, Y., Ouillon, G., Woessner, J., Sornette, D., & Husen, S. (2013). Automatic reconstruction of fault networks from seismicity catalogs including location uncertainty. *Journal of Geophysical Research: Solid Earth*, 118(11), 5956–5975. https://doi.org/10.1002/2013jb010164
- Williams-Stroud, S., Ozgen, C., & Billingsley, R. L. (2013). Microseismicity-constrained discrete fracture network models for stimulated reservoir simulation. Geophysics, 78(1), B37–B47. https://doi.org/10.1190/geo2011-0061.1
- Wu, H., Fu, P., Hawkins, A. J., Tang, H., & Morris, J. P. (2021). Predicting thermal performance of an enhanced geothermal system from tracer tests in a data assimilation framework. *Water Resources Research*, 57(12), e2021WR030987. https://doi.org/10.1029/2021wr030987
- Zha, Y., Yeh, T.-C. J., Illman, W. A., Tanaka, T., Bruines, P., Onoe, H., & Saegusa, H. (2015). What does hydraulic tomography tell us about fractured geological media? A field study and synthetic experiments. *Journal of Hydrology*, 531, 17–30. https://doi.org/10.1016/j.ihydrol.2015.06.013
- Zhang, S., Jiang, Z., Zhang, S., Zhang, Q., & Feng, G. (2021). Well placement optimization for large-scale geothermal energy exploitation considering nature hydro-thermal processes in the Gonghe Basin, China. *Journal of Cleaner Production*, 317, 128391. https://doi.org/10.1016/j.iclepro.2021.128391
- Zhao, H., Luo, N., & Illman, W. A. (2021). The importance of fracture geometry and matrix data on transient hydraulic tomography in fractured rocks: Analyses of synthetic and laboratory rock block experiments. *Journal of Hydrology*, 601, 126700. https://doi.org/10.1016/j.jhydrol.2021.126700
- Ziegler, M., Valley, B., & Evans, K. F. (2015). Characterization of natural fractures and fracture zones of the Basel EGS reservoir inferred from geophysical logging of the Basel-1 well, paper presented at World Geothermal Congress Melbourne, Australia.
- Zoback, M. D., Barton, C., Brudy, M., Castillo, D., Finkbeiner, T., Grollimund, B., et al. (2003). Determination of stress orientation and magnitude in deep wells. *International Journal of Rock Mechanics and Mining Sciences*, 40(7–8), 1049–1076. https://doi.org/10.1016/j.ijrmms.2003.07.001

JIANG ET AL. 22 of 22